J. Mech. Phys. Solids 209 (2026) 106499

Contents lists available at ScienceDirect

Journal of the Mechanics and Physics of Solids

journal homepage: www.elsevier.com/locate/jmps

A unified multi-perspective quadratic manifold for mitigating the Kolmogorov barrier in multiphysics damage

Qinghua Zhang[a,*], Stephan Ritzert[a], Jian Zhang[a], Jannick Kehls[a], Stefanie Reese[a,b], Tim Brepols[a]

[a] Institute of Applied Mechanics, RWTH Aachen University, Mies-van-der-Rohe-Str. 1, 52074, Aachen, Germany
[b] University of Siegen, Adolf-Reichwein-Straße 2a, 57076, Siegen, Germany

ARTICLE INFO

Keywords:
Multi-field decomposition
Quadratic manifolds
Multi-state decomposition
Kolmogorov barrier
Multiphysics
Damage

ABSTRACT

In multiphysics damage problems, material degradation is often modeled using local and/or global damage variables, whose evolution introduces strong nonlinearities and significant computational costs. Linear projection-based reduced-order models (ROMs) are widely used to accelerate these simulations but often fail to capture complex nonlinear damage evolution effectively. This limitation arises from the slow decay of the Kolmogorov n-width, which leads to a phenomenon known as the Kolmogorov barrier in linear approximation. To overcome this challenge, this study proposes a novel unified multi-perspective (multi-field and multi-state) quadratic manifold-based ROM framework for thermo-mechanically coupled damage-plasticity problems. A key feature lies in a multi-field and multi-state decomposition strategy that is grounded in the material's physical response to guide the selection of mode numbers for each coupled field. Moreover, the framework decouples both material states and physical fields, providing clearer insights into the contributions and interactions of each field within the overall multiphysics simulation. Benchmark tests demonstrate that the proposed approach mitigates the Kolmogorov barrier of linear projection-based ROMs by ensuring a smooth and monotonic decrease in error as the number of modes increases. The proposed multi-perspective quadratic manifold framework offers a robust and flexible approach for efficiently reducing complex damage-involved multiphysics problems and shows the potential for industrial applications.

1. Introduction

Dimensional reduction, in physical problems often achieved by suitably projecting governing equations from the full-order space onto lower-dimensional subspaces, plays a critical role in accelerating computational simulations. However, many existing studies Radermacher and Reese (2016), Ghavamian et al. (2017), Rocha et al. (2020), Kastian et al. (2023) focus exclusively on linear projections and often neglect the fact that a high compressibility of the reduced order model relies heavily on a fast decay of the Kolmogorov n-width Pinkus (2012), Cohen et al. (2023), Barnett and Farhat (2022), Greif and Urban (2019). The Kolmogorov n-width limitation in model order reduction (MOR) arises when approximating complex high-dimensional systems using low-dimensional linear projections and is also called the Kolmogorov barrier Peherstorfer (2022). Simply speaking, certain nonlinear systems may not be well approximated using linear projection methods. This results in significant errors in reduced order modeling, for instance, problems involving shocks, discontinuities, or highly localized phenomena (e.g., damage Felder et al. (2022), Zhang et al. (2025a) or

* Corresponding author.
E-mail address: qinghua.zhang@rwth-aachen.de (Q. Zhang).

https://doi.org/10.1016/j.jmps.2025.106499
Received 21 August 2025; Received in revised form 17 November 2025; Accepted 28 December 2025
Available online 1 January 2026
0022-5096/

transport-dominated problems Peherstorfer (2020), Geelen et al. (2023b)), where it is particularly difficult to precisely capture the nonlinear effects using a low-dimensional linear subspace.

In light of the approximation barrier posed by the slow decay of the Kolmogorov n-width Greif and Urban (2019), Bachmayr and Cohen (2017), Barnett and Farhat (2022), Cohen et al. (2023), recent research has increasingly turned to nonlinear approximation techniques. These approaches aim to construct reduced models through nonlinear mappings that can better capture the system's complex behavior. As a result, noticeable interest has emerged in the development of nonlinear reduction techniques for finite element (FE)-based simulations due to the widespread application of FE in industry, see Rutzmoser et al. (2017), Jain et al. (2017), Jain and Tiso (2019), Ghavamian et al. (2017). In the FE framework, projection-based MOR denotes a semi-discretization, wherein global shape and test functions are employed to construct either a Galerkin or Petrov-Galerkin projection to the governing equations Barnett and Farhat (2022). This process is realized by collecting and compressing solution snapshots of a discretized equation system using a *thin* singular value decomposition (SVD) to build up a reduced-order basis (ROB). Once the ROB is obtained, the global shape and test functions can be chosen either to be the same or different. If these functions are identical, the resulting formulation corresponds to a Galerkin projection, in which the governing equations are projected onto the reduced subspace. If they differ, a Petrov-Galerkin projection is applied instead. In the context of nonlinear approximation, not only the classical linear projection quantities but also both the nonlinear projection matrix and the quadratic/higher-order operator are needed Geelen et al. (2024, 2023a). Such projection-based MOR approaches are commonly referred to as *manifold learning* or *simulation-driven* computational methods, see Barnett and Farhat (2022), Geelen et al. (2023b), Jain and Tiso (2019), Lee and Verleysen (2007).

Over the past few decades, projection-based MOR has achieved significant success in both solid mechanics Ghavamian et al. (2017), Kaneko et al. (2021), Ghnatios et al. (2024), Michel and Suquet (2016), Farhat et al. (2015, 2014) and fluid mechanics Grimberg et al. (2021), Tezaur et al. (2022), Grimberg et al. (2020), Washabaugh et al. (2012), Barnett and Farhat (2022). In solid mechanics, many studies have focused on materials for which the Kolmogorov n-width decays rapidly, such as hyperelastic Radermacher and Reese (2013), Bhattacharjee and Matouš (2016), Goury and Duriez (2018), plastic Lange et al. (2024), Bugas and Runnels (2024), and viscoelastic Radermacher and Reese (2016, 2013), Trainotti et al. (2024) materials. As the governing partial differential equations (PDEs) in these models are typically weakly nonlinear, standard single-field-based proper orthogonal decomposition (POD) methods can efficiently compress solution snapshots of both linear ordinary differential equations (ODEs) and weakly nonlinear PDEs. In contrast, for damage models typically characterized by a slow decay of the Kolmogorov n-width, reduced-order modeling remains considerably more challenging. Few studies have successfully developed reduced-order approaches that can accurately capture the global softening behavior induced by damage. For complex multiphysics-coupled damage models, the available literature is rare and remains under-investigated. Within the context of reduced-order modeling in finite element simulations, the overall strategies can be broadly classified into two categories: general model order reduction approaches globally decreasing the number of degrees of freedom (e.g., via projection-based techniques such as POD Radermacher and Reese (2013), Ghavamian et al. (2017), Zhang et al. (2025a)) and hyperreduction (e.g., through element or quadrature point sampling to further reduce computational costs Hernandez et al. (2017), Lange et al. (2024), Wulfinghoff (2025)). A deep investigation of the limitations imposed by approximation theory is essential to understand the mechanisms behind instabilities that may occur when applying such reduction strategies. For instance, in damage-induced softening simulations, many studies do not focus enough on the slow decay of the Kolmogorov n-width and its underlying mechanisms. The problem usually becomes even more pronounced if multi-physical coupling effects play a role. In such cases, employing a standard single-field-based linear projection theory can lead to strong fluctuations in the reduced-order solution, particularly in the softening region, see Selvaraj and Hallett (2024), Kastian et al. (2023), Mishra et al. (2024), Rocha et al. (2020), Oliver et al. (2017).

To mitigate the Kolmogorov barrier, nonlinear manifolds (quadratic or of higher order) were developed to accurately represent the strongly nonlinear character of the governing equations. To the best of the authors' knowledge, the well-accepted contribution of Qiao et al. (2012) pioneered the use of nonlinear mapping for dimensional reduction through manifold learning in computer science. Subsequently, a quadratic manifold MOR approach was developed by Jain et al. (2017) for structural dynamic problems discretized by finite elements. Their approach outperformed linear projections that fail to capture the rapid degradation of the dynamic response. In the same year, Rutzmoser et al. (2017) extended the quadratic manifold method by incorporating static derivatives to generalize modal derivatives for the displacement field, which improves the accuracy of the quadratic manifold approach in engineering problems. Nevertheless, despite its efficacy in mitigating the Kolmogorov barrier and providing more precise projections, an achievable reduction in computation time remains limited in nonlinear finite element simulations, since the repeated calculation of the full global stiffness matrix and residual vector is still required.

To overcome this, Jain and Tiso (2019) built upon An et al. (2008)'s initial presentation of the energy-conserving sampling and weighting (ECSW) method in computer graphics as well as Farhat et al. (2014, 2015)'s extension of ECSW-based hyperreduction for solid mechanics by combining ECSW with the quadratic manifold framework for structural dynamics. Jain and Tiso (2019) further provided a rigorous proof that ECSW conserves energy and preserves the Lagrangian structure dictated by Hamilton's principle, ensuring intrinsic numerical stability in time integration. Subsequently, Barnett and Farhat (2022) consistently applied a similar ECSW-based manifold coupling strategy in the context of fluid mechanics with promising results. In their work, the slow decay of the Kolmogorov n-width for the simulation of the Ahmed body's turbulent wake flow Ahmed et al. (1984) was emphasized. However, the distribution of the Kolmogorov n-width was, in the authors' opinion, not clearly enough presented. Subsequently, Geelen et al. (2023b, 2024, 2023a) extended the quadratic manifold approach to address the slow decay of the Kolmogorov n-width in transport-dominated dynamic problems, yielding promising accuracy via a purely data-driven methodology. Through this non-intrusive approach, constant, linear, and nonlinear operators are determined by minimizing the difference between high-fidelity and approximated solutions, without direct access to stiffness matrices and discretized residuals. However, it should be noted that this approach relies heavily on nonlocal data inference, and its applicability to damage-plasticity models, characterized by numerous local variables and complex global-local coupling, remains unexplored. Furthermore, many studies have demonstrated the instabilities that can arise while using reduced-order damage models, once damage-induced global softening occurs in the material Oliver et al. (2017), Kerfriden et al. (2011, 2013), Selvaraj and Hallett (2024), Rocha et al. (2020), Kastian et al. (2023).

To overcome these instabilities, the reduced space can be enriched by non-converged solutions to facilitate convergence, as shown by Hernández et al. (2014), Radermacher and Reese (2016). However, this inevitably requires a larger number of modes to achieve sufficient enrichment of the subspace. Instead, Zhang et al. (2025a) proposed an effective strategy using a multi-field decomposed approach based on linear projection. In their work, based on the vectoral equivalence of the discretized multiphysics solutions, the multi-field decomposed approach is realized by individually projecting the governing equations of each physical field onto distinct subspaces at a global level. However, this approach still requires a relatively large number of modes across multiple fields due to the inherent limitations of the linear approximation, which is particularly affected by the slow decay of the Kolmogorov n-width in the associated solution spaces. In addition, the POD-based Galerkin method employed there remains constrained by the computational bottleneck associated with the repeated evaluation of all elements during the iterative procedures. To overcome these challenges, a novel unified multi-field and multi-state decomposed quadratic manifold MOR formulation is proposed in this work to effectively mitigate the Kolmogorov barrier observed in multi-physical damage problems in a fast manner. To realize a fast simulation for strongly nonlinear problems, the approach is additionally integrated with the ECSW-based hyperreduction technique. The new method aims to significantly reduce the computational cost of thermo-mechanically coupled damage-plasticity simulations.

In light of the observations above, the paper is structured as follows. Section 2 briefly provides the derivation of a thermo-mechanically coupled gradient-extended damage model along with its governing partial differential equations. Section 3 provides a mathematical analysis of the slow decay of the Kolmogorov n-width associated with the considered multi-physical damage model. A novel unified quadratic manifold-based MOR framework is then proposed, incorporating a multi-field and multi-state decomposition together with a corresponding ECSW-based hyperreduction technique to mitigate the Kolmogorov barrier in damage. Section 4 investigates the performance of the newly proposed MOR approach through two academic benchmark problems, focusing on reduction efficiency, predictive accuracy, and numerical precision. Section 5 conducts a comparative error analysis between the decomposed and non-decomposed strategies applied to the coefficient matrices, highlighting the critical role of field-wise decomposition. Furthermore, a comparison is carried out between the quadratic manifold-based method and a classical POD-based linear approximation, aiming to explain why the quadratic manifold is preferred in the reduced-order modeling of multi-physical damage simulations. Finally, Section 6 summarizes the key findings, discusses the advantages and limitations of the newly proposed MOR approach, and outlines potential directions for future research.

2. Material model

2.1. Kinematics and general form of the Helmholtz free energy density function

Following the multiplicative decomposition framework proposed by Lu and Pister (1975), the deformation gradient $\boldsymbol{F}$ is multiplicatively decomposed into a mechanical part $\boldsymbol{F}_m$ and a thermal part $\boldsymbol{F}_\theta$ Stojanovic et al. (1964). The mechanical part $\boldsymbol{F}_m$ is further decomposed into elastic and plastic components, denoted by $\boldsymbol{F}_e$ and $\boldsymbol{F}_p$, respectively:

$$\boldsymbol{F} = \boldsymbol{F}_m\,\boldsymbol{F}_\theta = \boldsymbol{F}_e\,\boldsymbol{F}_p\,\boldsymbol{F}_\theta \quad \text{with} \quad \boldsymbol{F}_\theta = \underbrace{\exp\left(\alpha\left(\theta - \theta_0\right)\right)}_{\vartheta(\theta)}\,\boldsymbol{I}. \tag{1}$$

Here, under the assumption of isotropic thermal expansion, the thermal deformation gradient $\boldsymbol{F}_\theta$ can be expressed in terms of an exponential function $\vartheta(\theta)$ that depends on the temperature θ, see Stojanovic et al. (1964). Eq. (1) involves the reference temperature θ_0 and the second-order identity tensor $\boldsymbol{I}$. The parameter α denotes the thermal expansion coefficient which is assumed to be temperature-independent. Based on the underlying kinematic relations, the elastic and plastic right Cauchy-Green tensors are expressed as:

$$\boldsymbol{C}_e = \boldsymbol{F}_e^{\mathrm{T}}\,\boldsymbol{F}_e = \frac{1}{\vartheta^2}\,\boldsymbol{F}_p^{-\mathrm{T}}\,\boldsymbol{C}\,\boldsymbol{F}_p^{-1}, \quad \boldsymbol{C}_p = \boldsymbol{F}_p^{\mathrm{T}}\,\boldsymbol{F}_p. \tag{2}$$

Subsequently, the general Helmholtz free energy density function per unit reference volume ψ is assumed to depend on the elastic and plastic right Cauchy-Green tensors, denoted by $\boldsymbol{C}_e$ and $\boldsymbol{C}_p$, respectively, as well as the temperature θ in the following way:

$$\psi = \underbrace{f_d(D)\big(\psi_e\,(\boldsymbol{C}_e,\,\theta) + \psi_p\,(\boldsymbol{C}_p,\,\xi_p,\,\theta)\big)}_{\text{Elastoplastic part}} + \underbrace{\psi_d\,(\xi_d,\,\theta)}_{\text{Damage hardening part}} + \underbrace{\psi_{\bar{d}}\,(D,\,\bar{D},\,\nabla\bar{D},\,\theta)}_{\text{Micromorphic extension}} + \underbrace{\psi_\theta\,(\theta)}_{\text{Caloric part}}. \tag{3}$$

Based on the hypothesis of energy equivalence proposed by Cordebois and Sidoroff (1982), a quadratic degradation function $f_d(D) = (1-D)^2$ is used to degrade the elastoplastic energy whenever the local damage variable D evolves. ψ_e represents the elastic energy density, which depends on both the elastic right Cauchy-Green tensor $\boldsymbol{C}_e$ and temperature θ. ψ_p denotes the plastic energy density, which is formulated in terms of the plastic right Cauchy-Green tensor $\boldsymbol{C}_p$, the accumulated plastic strain ξ_p, and the temperature θ. In addition, a damage-hardening energy density ψ_d is postulated as a function of the damage-hardening variable ξ_d and the temperature θ.

Following the general micromorphic framework proposed by Forest (2009), the energy density contribution $\psi_{\bar{d}}$ introduces a coupling between the local damage variable D and the nonlocal (micromorphic) damage variable $\bar{D}$. It also incorporates the influence of its gradient $\nabla\bar{D}$, defined with respect to the reference configuration. In the present work, the caloric energy density ψ_θ does not require a further specification for certain temperature-dependent materials Ames et al. (2009), Zhang et al. (2022), Ruan et al. (2024) , as a constant heat capacity (c:=const.) is assumed.

Further details are omitted here for brevity; interested readers are referred to Felder et al. (2022). The energy density is formulated in terms of the invariants of $\boldsymbol{C}_e$, which can alternatively be expressed in terms of $\boldsymbol{C}$ and $\boldsymbol{C}_p$, see Eq. (2). Accordingly, the total Helmholtz free energy density function is expressed as $\psi(\boldsymbol{C}, \zeta_{\text{int}}, \bar{D}, \nabla\bar{D}, \theta)$, where the internal variables are defined as $\zeta_{\text{int}} := \{\boldsymbol{C}_p, \xi_p, D, \xi_d\}$.

2.2. Specific choice for the Helmholtz free energy density

- Elastoplasticity

A compressible Neo-Hookean-type material model is adopted for the elastic energy density function ψ_e, which is defined in terms of the elastic right Cauchy-Green tensor $\boldsymbol{C}_e$ as:

$$\psi_e = \frac{\mu}{2}\left(\text{tr}(\boldsymbol{C}_e) - 3 - \ln\left(\det\left(\boldsymbol{C}_e\right)\right)\right) + \frac{\Lambda}{4}\left(\det\left(\boldsymbol{C}_e\right) - 1 - \ln\left(\det\left(\boldsymbol{C}_e\right)\right)\right). \tag{4}$$

The plastic energy density function ψ_p is expressed as follows:

$$\psi_p = \underbrace{\frac{a}{2}\left(\text{tr}(\boldsymbol{C}_p) - 3 - \ln\left(\det(\boldsymbol{C}_p)\right)\right)}_{\text{linear kinematic hardening}} + \underbrace{e_p\left(\xi_p + \frac{\exp(-f_p\,\xi_p) - 1}{f_p}\right)}_{\text{nonlinear isotropic hardening}} + \underbrace{\frac{1}{2}\,P\,\xi_p^2}_{\text{linear isotropic hardening}}. \tag{5}$$

Here, the Lamé constants μ and Λ in Eq. (4) as well as the plastic material parameters a, e_p, f_p, and P in Eq. (5) can be temperature dependent.

- Damage hardening

The energy density function associated with damage hardening is defined in analogy to the nonlinear isotropic hardening in plasticity, with e_d and f_d denoting constant material parameters:

$$\psi_d = e_d\left(\xi_d + \frac{\exp(-f_d\,\xi_d) - 1}{f_d}\right). \tag{6}$$

- Micromorphic extension

$$\psi_{\bar{d}} = \underbrace{\frac{H}{2}\left(D - \bar{D}\right)^2}_{\text{local - nonlocal coupling}} + \frac{A}{2}\,\nabla\bar{D}\cdot\nabla\bar{D} \tag{7}$$

The micromorphic energy density function $\psi_{\bar{d}}$ introduces a strong coupling between the local damage variable D and the nonlocal damage variable $\bar{D}$ through a constant penalty parameter H, as proposed by Forest (2009). Furthermore, the constant material parameter A serves as a length scale relevant parameter that governs the contribution of the gradient term $\nabla\bar{D}$, the latter of which provides an appropriate regularization of the formulation. The presented model is thermodynamically consistent. Further details are omitted at this point, but can be found in Brepols et al. (2018, 2020), Felder et al. (2022) or Appendix A .

2.3. Balance equations

The material model in this study is based on the general micromorphic approach proposed by Forest (2009), which basically eliminates the well-known mesh dependency issues of conventional local continuum damage models. Under the assumption of quasi-static finite strain deformations and a transient thermal field, the corresponding partial differential equations governing the formulation are expressed as follows:

<u>Balance of linear momentum</u>

$$\begin{aligned} \text{Div}(\boldsymbol{F}\,\mathbf{S}) + \bar{\boldsymbol{f}} &= \boldsymbol{0} && \text{in } \Omega \\ (\boldsymbol{F}\,\mathbf{S})\cdot\boldsymbol{n} &= \bar{\boldsymbol{t}} && \text{on } \partial\Omega_t \\ \boldsymbol{u} &= \tilde{\boldsymbol{u}} && \text{on } \partial\Omega_u \end{aligned} \tag{8}$$

<u>Micromorphic balance</u>

$$\begin{aligned} \text{Div}\left(\boldsymbol{b}_i - \boldsymbol{b}_e\right) - a_i + a_e &= 0 && \text{in } \Omega \\ \left(\boldsymbol{b}_i - \boldsymbol{b}_e\right)\cdot\boldsymbol{n} &= a_c && \text{on } \partial\Omega_c \\ \bar{D} &= \tilde{\bar{D}} && \text{on } \partial\Omega_{\bar{D}} \end{aligned} \tag{9}$$

Energy balance

$$
\begin{aligned}
\underbrace{-\dot{e}_{\text{int}} + \mathbf{S} : \frac{1}{2}\dot{\boldsymbol{C}} + a_i\,\dot{\bar{D}} + \boldsymbol{b}_i \cdot \nabla\dot{\bar{D}}}_{r_{\text{int}}} + r_{\text{ext}} - \operatorname{Div}(\boldsymbol{q}) &= 0 && \text{in } \Omega \\
\boldsymbol{q}\cdot\boldsymbol{n} &= -\bar{q} && \text{on } \partial\Omega_q \\
\theta &= \widetilde{\theta} && \text{on } \partial\Omega_\theta
\end{aligned}
\tag{10}
$$

In the above balance equations, Ω denotes the domain of the body in the reference configuration. $\mathbf{S}$ represents the second Piola-Kirchhoff stress tensor. Eq. (9) formulates the micromorphic balance in terms of the internal body forces a_i and $\boldsymbol{b}_i$, as well as the external micromorphic forces a_e and $\boldsymbol{b}_e$. In the present formulation, a_e and $\boldsymbol{b}_e$ are assumed to be zero. The vector $\bar{\boldsymbol{f}}$ denotes the general body force per unit reference volume, while $\boldsymbol{n}$ represents the unit outward normal vector. In Eq. (10), the internal energy per unit reference volume e_{int} and its time derivative $\dot{e}_{\text{int}}$ are given by $e_{\text{int}} = \psi + \theta\,\eta$ and $\dot{e}_{\text{int}} = \dot{\psi} + \dot{\theta}\,\eta + \theta\,\dot{\eta}$, respectively. The entropy and volumetric heat capacity are defined as $\eta = -\frac{\partial\psi}{\partial\theta}$ and $c = -\frac{\partial^2\psi}{\partial\theta^2}$, respectively. Assuming a constant heat capacity and no external heat source ($r_{\text{ext}} = 0$), this leads to $\dot{e}_{\text{int}} = c\,\dot{\theta}$, see Appendix B for details. On the Dirichlet boundaries $\partial\Omega_u$, $\partial\Omega_{\bar{D}}$, and $\partial\Omega_\theta$, displacements $\widetilde{\boldsymbol{u}}$, nonlocal damage $\widetilde{\bar{D}}$, and temperature $\widetilde{\theta}$ are prescribed, respectively. Similarly, Neumann boundary conditions are imposed on $\partial\Omega_t$, $\partial\Omega_c$, and $\partial\Omega_q$, associated with the macroscopic traction force $\bar{\boldsymbol{t}}$, the micromorphic traction force a_c, and the heat flux $\bar{q}$, respectively. The total internal heat generation is subsequently expressed as $r_{\text{int}} = r_e + r_p + r_d$, where r_e, r_p, and r_d denote the elastic, plastic, and damage-related contributions, respectively. Further details can be found in Felder et al. (2022) and Reese (2001).

2.4. Weak form of the problem

Based on the strong form given in Eqs. (8), (9), and (10), the corresponding weak form is obtained by multiplying the equations with appropriate test functions, namely $\delta\boldsymbol{u}$, $\delta\bar{D}$, and $\delta\theta$. The energy residuals for an element associated with the displacement, damage, and temperature fields[1] are denoted as g_u^e, g_d^e, and g_θ^e, respectively:

- Displacement field

$$
g_u^e(\boldsymbol{u},\, \bar{D},\, \theta, \delta\boldsymbol{u}) = \int_{\Omega_e} \mathbf{S} : \delta\boldsymbol{E}\,dV - \int_{\Omega_e} \bar{\boldsymbol{f}}\cdot\delta\boldsymbol{u}\,dV - \int_{\partial\Omega_e} \bar{\boldsymbol{t}}\cdot\delta\boldsymbol{u}\,dA \tag{11}
$$

- Damage field

$$
g_d^e(\boldsymbol{u},\, \bar{D},\, \theta,\, \delta\bar{D}) = \int_{\Omega_e} H\left(D - \bar{D}\right)\delta\bar{D}\,dV - \int_{\Omega_e} A\,\nabla\bar{D}\cdot\nabla(\delta\bar{D})\,dV \tag{12}
$$

- Temperature field

$$
g_\theta^e(\boldsymbol{u},\, \bar{D},\, \theta,\, \dot{\theta},\, \delta\theta) = \int_{\Omega_e} c\,\dot{\theta}\,\delta\theta\,dV - \int_{\Omega_e} \boldsymbol{q}\cdot\nabla(\delta\theta)\,dV - \int_{\Omega_e} r_{\text{int}}\,\delta\theta\,dV - \int_{\partial\Omega_e} \bar{q}\,\delta\theta\,dA \tag{13}
$$

Here, $\partial\Omega_e$ represents the relevant Dirichlet ($\partial\Omega_{e,D} = \partial\Omega_{e,u} \cup \partial\Omega_{e,\bar{D}} \cup \partial\Omega_{e,\theta}$) and Neumann ($\partial\Omega_{e,N} = \partial\Omega_{e,t} \cup \partial\Omega_{e,c} \cup \partial\Omega_{e,q}$) boundaries of an element e, with $\partial\Omega_e = \partial\Omega_{e,D} \cup \partial\Omega_{e,N}$. For brevity, a unified boundary $\partial\Omega_e$ is employed here. $\delta\boldsymbol{E} = \frac{1}{2}\left[\boldsymbol{F}^{\mathrm{T}}\,\nabla(\delta\boldsymbol{u}) + \nabla^{\mathrm{T}}(\delta(\boldsymbol{u}))\,\boldsymbol{F}\right]$ denotes the test function of the Green-Lagrange strain tensor $\delta\boldsymbol{E}$. The element residual force $\boldsymbol{R}_e$ is derived from the virtual energy $g^e = g_u^e + g_d^e + g_\theta^e$ with respect to all element degrees of freedom $\boldsymbol{U}_e = [\boldsymbol{u},\, \bar{D},\, \theta]$, named the displacement $\boldsymbol{u}$, nonlocal damage $\bar{D}$, and temperature θ:

$$
\boldsymbol{R}_e = \frac{\partial g^e\,(\boldsymbol{u},\, \bar{D},\, \theta)}{\partial\boldsymbol{U}_e}, \quad \boldsymbol{K}^e = \frac{\partial\boldsymbol{R}_e\,(\boldsymbol{u},\, \bar{D},\, \theta)}{\partial\boldsymbol{U}_e}. \tag{14}
$$

Specifically, the residual force vector is obtained by taking the partial derivative of the virtual energy g^e with respect to the nodal degrees of freedom. Subsequently, the element stiffness matrix $\boldsymbol{K}^e$ is obtained by the partial derivative of the residual vector $\boldsymbol{R}_e$ with respect to the nodal degrees of freedom. Accordingly, the components of the element stiffness matrix $\boldsymbol{K}^e$ are expressed as follows:

$$
\boldsymbol{K}_{uu}^e = \frac{\partial^2 g^e}{\partial\boldsymbol{u}^2},\ \boldsymbol{K}_{u\bar{D}}^e = \frac{\partial^2 g^e}{\partial\boldsymbol{u}\partial\bar{D}},\ \boldsymbol{K}_{u\theta}^e = \frac{\partial^2 g^e}{\partial\boldsymbol{u}\partial\theta},\ K_{\bar{D}\bar{D}}^e = \frac{\partial^2 g^e}{\partial\bar{D}^2},\ K_{\bar{D}\theta}^e = \frac{\partial^2 g^e}{\partial\bar{D}\partial\theta},\ K_{\theta\theta}^e = \frac{\partial^2 g^e}{\partial\theta^2}. \tag{15}
$$

[1] Note that the field quantities in the following belong to an element e and should probably more precisely be denoted as $\boldsymbol{u}^e$, $\bar{D}^e$, and θ^e. However, this is intentionally avoided to prevent a proliferation of notation, and instead understood implicitly.

The omitted matrices $\boldsymbol{K}^e_{\bar{D}u}$, $\boldsymbol{K}^e_{\theta u}$, and $K^e_{\theta\bar{D}}$ are derived analogously. Derivatives are computed by the automated differentiation toolbox *AceGen* Korelc (2002), Korelc and Wriggers (2016). The global residual vector $\boldsymbol{R}$, stiffness matrices $\boldsymbol{K}$, and increment vectors of unknowns $\Delta\boldsymbol{U}$ are then assembled from their corresponding element-level counterparts $\boldsymbol{R}_e$, $\boldsymbol{K}^e$, and $\Delta\boldsymbol{U}_e$, respectively, as follows:

$$\boldsymbol{R} = \mathop{\mathbf{A}}_{e=1}^{N_e} \boldsymbol{R}_e, \quad \boldsymbol{K} = \mathop{\mathbf{A}}_{e=1}^{N_e} \boldsymbol{K}^e, \quad \Delta\boldsymbol{U} = \mathop{\mathbf{A}}_{e=1}^{N_e} \Delta\boldsymbol{U}_e, \tag{16}$$

where the operator $\mathop{\mathbf{A}}_{e=1}^{N_e}(\bullet)$ in Eq. (16) denotes the well-known assembly operator applied to all elements N_e in the given domain. Finally, the global stiffness matrix $\boldsymbol{K}$, the residual force vector $\boldsymbol{R}$, and the increment of the global solution vector $\Delta\boldsymbol{U}$ are expressed as:

$$\underbrace{\begin{pmatrix} \boldsymbol{K}_{uu} & \boldsymbol{K}_{u\bar{D}} & \boldsymbol{K}_{u\theta} \\ \boldsymbol{K}_{\bar{D}u} & \boldsymbol{K}_{\bar{D}\bar{D}} & \boldsymbol{K}_{\bar{D}\theta} \\ \boldsymbol{K}_{\theta u} & \boldsymbol{K}_{\theta\bar{D}} & \boldsymbol{K}_{\theta\theta} \end{pmatrix}}_{\boldsymbol{K}} \underbrace{\begin{pmatrix} \Delta\boldsymbol{u} \\ \Delta\bar{\boldsymbol{D}} \\ \Delta\boldsymbol{\theta} \end{pmatrix}}_{\Delta\boldsymbol{U}} = -\underbrace{\begin{pmatrix} \boldsymbol{R}_u \\ \boldsymbol{R}_{\bar{D}} \\ \boldsymbol{R}_\theta \end{pmatrix}}_{\boldsymbol{R}}. \tag{17}$$

3. Nonlinear manifold model order reduction

In a nonlinear finite element computation based on the Newton-Raphson method, Eq. (17) needs to be solved repeatedly for the high-dimensional increment vector $\Delta\boldsymbol{U}$. However, this approach can become computationally expensive, particularly for damage problems where a large number of finite elements are usually required. Therefore, projection-based MOR techniques are employed to enable more efficient simulations.

3.1. Reducibility of Kolmogorov n-width barrier in damage

In the case of damage problems, when the local damage initiates, the associated stress tensors are degraded by a quadratic degradation function $f_d(D) = (1 - D)^2$, see Eqs. (3), (A.3), (A.4), and (A.5). In more complex scenarios, incorporating the spectral decomposition for the stress tensor to distinguish the tensile and compressive responses in an asymmetric manner results in a highly nonlinear constitutive relation Fassin et al. (2019), Zhang et al. (2025b), Wu (2017), Jiang et al. (2025), Ruan et al. (2023), Miehe et al. (2010), Narayan and Anand (2021). The high nonlinearity of the presented themo-mechanically coupled damage-plasticity model typically leads to the phenomenon that the singular values of the snapshot matrix decay very slowly during the entire simulation process, see Fig. C.17 in Appendix C.

The slow decay of the singular values is analogous to the decay of the Kolmogorov n-width, thereby introducing a Kolmogorov barrier Greif and Urban (2019), Peherstorfer (2022), Barnett and Farhat (2022), Geelen et al. (2023b), Cohen et al. (2023). This poses a challenge for approximations based on a linear projection method. The Kolmogorov n-width with the dimension of the subspace n is defined as:

$$d_n(\boldsymbol{\mathcal{S}}) := \inf_{\substack{\mathcal{Y}_n \subseteq \mathcal{Y} \\ \dim(\mathcal{Y}_n) \leq n}} \sup_{\boldsymbol{u} \in \boldsymbol{\mathcal{S}}} \inf_{\boldsymbol{u}_n \in \mathcal{Y}_n} \|\boldsymbol{u} - \boldsymbol{u}_n\|_{\mathcal{Y}}, \tag{18}$$

which formulates the maximum distance between the manifold solution point $\boldsymbol{u}$ and the reconstructed solution point $\boldsymbol{u}_n$ while projecting the solution points of $\boldsymbol{\mathcal{S}}$ onto a Hilbert or Banach space $\mathcal{Y}$ by incorporating the supremum and the second infimum. Here, $\boldsymbol{\mathcal{S}}$ denotes a set of collected solutions of PDEs and is therefore named *solution manifold*. $\mathcal{Y}_n$ represents the linear subspace Greif and Urban (2019), Barnett and Farhat (2022). For certain linear coercive parameterized problems, the Kolmogorov n-width d_n decays drastically and exhibits an exponential decay according to $d_n \leq C\, e^{-\beta\, n}$, where $0 < C < \infty$ and $\beta > 0$ Buffa et al. (2012), Greif and Urban (2019), Ohlberger and Rave (2015). A fast decay of d_n indicates that the equation system is highly reducible using a linear projection-based method. However, in the case of elliptic or parabolic PDEs, d_n typically decays very slowly since $d_n \geq 1/4\,(n^{-1/2})$ Greif and Urban (2019), Barnett and Farhat (2022). The difference between the Kolmogorov n-width and the singular values should be shortly clarified. The Kolmogorov n-width is a discrepancy measure used to quantify the best achievable linear approximation error for a continuous $\boldsymbol{\mathcal{S}}$. The singular values are obtained by performing a singular value decomposition of the snapshot matrix $\boldsymbol{U}_{\text{snap}}$ to measure the error of the best n-dimensional linear approximation $\boldsymbol{U}_n$, i.e., $||\boldsymbol{U}_{\text{snap}} - \boldsymbol{U}_n||_F^2 = \sum_{i>n} \sigma_i^2$. The singular values of the snapshot matrix provide a numerical estimate of this for a finite sample of $\boldsymbol{\mathcal{S}}$. For a finite-dimensional data set of discretized $\boldsymbol{\mathcal{S}}$ equipped with the L^2 norm, the Kolmogorov n-width reads $d_n(\boldsymbol{\mathcal{S}}) = \sigma_{n+1}$ Unger and Gugercin (2019), Bachmayr and Cohen (2017). σ_{n+1} denotes the $(n+1)$-th singular value of the discretized solution manifold. Consequently, the decay of the singular value can be regarded as a discrete analog of the Kolmogorov n-with in certain cases. In other words, if the singular values decay rapidly, the PDE system is highly reducible. In this case, an accurate linear approximation is achievable using a low-dimensional reduced basis $\mathcal{Y}_n$. Conversely, if d_n decays slowly, a linear approximation method lacks the accuracy to reduce the equation system, leading to the Kolmogorov barrier in approximation, see the distribution of the normalized singular values in Fig. 4(a) and Appendix C.

In this study, the presence of a Kolmogorov n-width approximation barrier in the thermo-mechanically coupled damage-plasticity formulation arises from the type and nature of the governing PDEs. The corresponding solution manifold is highly nonlinear and spatially localized in certain regions.

More specifically, the mechanical equilibrium Eq. (8) for displacement and the balance Eq. (9) for micromorphic damage are elliptic Ostwald et al. (2019), while the transient heat conduction Eq. (10) is parabolic Mersel et al. (2025), Ostwald et al. (2019). Additionally, the micromorphic balance equation leads to a second-order spatial regularization. Despite the smoothing effect of the nonlocal gradient term, the damage field often exhibits strong spatial localization, such as sharp crack-like zones, whose location, orientation, and intensity can vary significantly for different parameters, e.g., the damage threshold Y_0, penalty parameter H, and gradient parameter A. The localized features result from the softening and coupling among the different field quantities, making the solution manifold strongly nonlinear. Even small variations in the input parameters can easily lead to qualitatively different damage patterns (e.g., distinct crack paths). A linear subspace cannot suitably capture these features. To mitigate the Kolmogorov barrier in linear projection, a new multi-perspective nonlinear manifold MOR approach is developed in this study with the intention to significantly accelerate multi-physical damage simulations.

3.2. Nonlinear manifolds for dimensionality reduction

Dimension reduction using nonlinear representation is realized by enriching linear approximations via low-order polynomial terms, which are dependent on the reduced state $\widetilde{\boldsymbol{U}}$ in the subspaces. To the authors' knowledge, the original work for nonlinear manifolds can be traced back to Qiao et al. (2012). Recently, numerous applications of nonlinear manifold MOR based on the single-field projection have been presented in Rutzmoser et al. (2017), Benner et al. (2020), Barnett and Farhat (2022), Geelen et al. (2023b), Zhang et al. (2024), Geelen et al. (2024). The objective of the nonlinear manifold MOR is to seek a mapping $\boldsymbol{\Gamma}(\bullet)$ that can approximate full states $\boldsymbol{U} \in \mathbb{R}^n$ via reduced states $\widetilde{\boldsymbol{U}} \in \mathbb{R}^r$ in a nonlinear manner as follows:

$$\boldsymbol{U} \approx \boldsymbol{\Gamma}(\widetilde{\boldsymbol{U}}) := \underbrace{\boldsymbol{\Phi}_{\mathrm{lin}}\,\widetilde{\boldsymbol{U}}}_{\text{linear}} + \underbrace{\bar{\boldsymbol{\Phi}}_{\mathrm{nonlin}}\,(\widetilde{\boldsymbol{U}} \otimes \widetilde{\boldsymbol{U}})}_{\text{nonlinear}}, \tag{19}$$

where $\boldsymbol{\Phi}_{\mathrm{lin}} \in \mathbb{R}^{n \times r}$ and $\bar{\boldsymbol{\Phi}}_{\mathrm{nonlin}} \in \mathbb{R}^{n \times q}$ denote linear and nonlinear projection matrices, respectively. n is the number of degrees of freedom in a discretized equation system, and r denotes the selected column number of the global linear projection matrices. Note that the operator $\otimes$ represents the Kronecker product[2] between two vectors. q[3] specifies the number of selected columns in the global nonlinear projection matrices. Here, unlike dynamic cases, the reference state $\boldsymbol{U}_{\mathrm{ref}}$ (initial condition) is not further discussed in the quasi-static case in this study, as shown in Geelen et al. (2023a), Benner et al. (2023), Jain and Tiso (2019), Jain et al. (2017). Since the initial condition is addressed separately within the Newton iteration, the primary focus is placed on the unknown quantities. Hence, following the pioneering contributions by Geelen et al. (2024, 2023a,b) in nonlinear manifold modeling, Eq. (19) is further simplified by introducing an additional coefficient matrix $\boldsymbol{\Xi} \in \mathbb{R}^{q \times (p-1)\,r}$ together with a polynomial operator $\boldsymbol{g}(\bullet)$, thereby avoiding the large computational cost associated with the Kronecker product. $\boldsymbol{\Xi}$ plays a key role in weighting the nonlinear projection basis and the higher-order polynomials of the reduced states:

$$\boldsymbol{U} \approx \boldsymbol{\Gamma}(\widetilde{\boldsymbol{U}}) := \boldsymbol{\Phi}_{\mathrm{lin}}\,\widetilde{\boldsymbol{U}} + \bar{\boldsymbol{\Phi}}_{\mathrm{nonlin}}\,\boldsymbol{\Xi}\,\boldsymbol{g}(\widetilde{\boldsymbol{U}}). \tag{20}$$

The operator $\boldsymbol{g}(\widetilde{\boldsymbol{U}})$ for the reduced state is expressed with the selected polynomial order p as:

$$\boldsymbol{g}(\widetilde{\boldsymbol{U}}) = \begin{pmatrix} \widetilde{\boldsymbol{U}}^2(t) \\ \vdots \\ \widetilde{\boldsymbol{U}}^p(t) \end{pmatrix} \tag{21}$$

As outlined by Volkwein (2013), Ghavamian et al. (2017), and Zhang et al. (2025a), the key idea of reduced-order modeling is to minimize the discrepancy between the full-order states and their reduced representations. This process aims to seek a mapping $\boldsymbol{\Gamma}$, which can be achieved in terms of a linear or nonlinear approach. As $\boldsymbol{\Gamma}$ is determined, it can be used to perform forward and backward projections between the high-fidelity space and the reduced subspace, enabling the reduced equations to be efficiently solved within the subspace. The minimization process is expressed in Eq. (22), where r_a represents the rank of the snapshot matrix and plays a key role in defining the dimension of the objective function:

$$\boldsymbol{\Gamma} = \underset{\{\boldsymbol{\Phi}_{\mathrm{lin}},\,\bar{\boldsymbol{\Phi}}_{\mathrm{nonlin}},\,\boldsymbol{\Xi}\}}{\arg\min} \sum_{j=1}^{r_a} \left\| \boldsymbol{U}_j - \boldsymbol{\Phi}_{\mathrm{lin}}\,\widetilde{\boldsymbol{U}}_j - \bar{\boldsymbol{\Phi}}_{\mathrm{nonlin}}\,\boldsymbol{\Xi}\,\boldsymbol{g}(\widetilde{\boldsymbol{U}}_j) \right\|_2^2. \tag{22}$$

To facilitate the minimization of Eq. (22), the error between the full-order (high-fidelity) states and their reduced representations is expressed using the Frobenius norm, denoted as $\mathcal{F}$. As demonstrated by Geelen et al. (2023b) as well as Grussler and Giselsson (2018), the regularized nuclear Frobenius norm is one of the most widely used for minimization problems, which aims to reduce the error while considering a huge amount of data. In this regard, $\mathcal{F}$ is expressed in terms of several quantities $\boldsymbol{\Phi}_{\mathrm{lin}}$, $\bar{\boldsymbol{\Phi}}_{\mathrm{nonlin}}$, $\boldsymbol{\Xi}$, and $\widetilde{\boldsymbol{U}}_{\mathrm{snap}}$ as:

$$\mathcal{F}\,(\boldsymbol{\Phi}_{\mathrm{lin}},\,\bar{\boldsymbol{\Phi}}_{\mathrm{nonlin}},\,\boldsymbol{\Xi},\,\widetilde{\boldsymbol{U}}_{\mathrm{snap}}) = \frac{1}{2} \left\| \boldsymbol{U}_{\mathrm{snap}} - \begin{bmatrix} \boldsymbol{\Phi}_{\mathrm{lin}} & \bar{\boldsymbol{\Phi}}_{\mathrm{nonlin}} \end{bmatrix} \begin{bmatrix} \widetilde{\boldsymbol{U}}_{\mathrm{snap}} \\ \boldsymbol{\Xi}\,\boldsymbol{g}(\widetilde{\boldsymbol{U}}_{\mathrm{snap}}) \end{bmatrix} \right\|_F^2. \tag{23}$$

[2] The Kronecker product of a vector $\boldsymbol{U}$ with itself is defined as $\boldsymbol{U} \otimes \boldsymbol{U} = [u_1^2, u_1 u_2, \cdots, u_1 u_n, u_2 u_1, u_2^2, \cdots, u_2 u_n, \cdots u_n^2]^{\mathrm{T}} \in \mathbb{R}^{n^2}$, where $\boldsymbol{U} = [u_1, u_2, \cdots u_n]^{\mathrm{T}} \in \mathbb{R}^n$. When duplicate elements are removed, the dimension of the product becomes $\boldsymbol{U} \otimes \boldsymbol{U} \in \mathbb{R}^{n(n+1)/2}$.

[3] Here, q can be expressed as $q = r^2$ or $q = r(r+1)/2$, depending on the chosen form of the Kronecker product. In this study, q is independent of r due to the employment of $\boldsymbol{\Xi}$.

Here, $\boldsymbol{U}_{\text{snap}} = [\boldsymbol{U}_1, \boldsymbol{U}_2, \dots \boldsymbol{U}_{n_{\text{step}}}] \in \mathbb{R}^{n \times n_{\text{step}}}$ is a snapshot matrix consisting of all converged nodal solutions of the precomputed full-order simulations. n_{step} denotes the step number of performed full-order simulations. In Eq. (23), the projection matrices need to be orthonormal as $\left(\boldsymbol{\Phi}_{\text{lin}}^{\text{T}}, \bar{\boldsymbol{\Phi}}_{\text{nonlin}}^{\text{T}}\right)^{\text{T}} (\boldsymbol{\Phi}_{\text{lin}}, \bar{\boldsymbol{\Phi}}_{\text{nonlin}}) = \boldsymbol{I}_{(r+q)}$, where $\boldsymbol{I}_{(r+q)}$ is the identity matrix with the dimension of $\mathbb{R}^{(r+q)\times(r+q)}$. This constraint forms a smooth submanifold of the subspace $\mathbb{R}^{n\times(r+q)}$, namely the Stiefel manifold Geelen et al. (2024). However, solely employing the Frobenius norm in Eq. (23) will lead to an overfitting problem in the minimization process Geelen et al. (2023b,a, 2024), especially when a huge amount of data is involved. To address this issue, an additional regularization in terms of the coefficient matrix Ξ is employed with a regularization parameter $\gamma \geq 0$ as:

$$\left\{\boldsymbol{\Phi}_{\text{lin}}, \bar{\boldsymbol{\Phi}}_{\text{nonlin}}, \Xi, \widetilde{\boldsymbol{U}}_{\text{snap}}\right\} = \underset{\{\boldsymbol{\Phi}_{\text{lin}}, \bar{\boldsymbol{\Phi}}_{\text{nonlin}}, \Xi, \widetilde{\boldsymbol{U}}_{\text{snap}}\}}{\arg\min} \left[\mathcal{F}(\boldsymbol{\Phi}_{\text{lin}}, \bar{\boldsymbol{\Phi}}_{\text{nonlin}}, \Xi, \widetilde{\boldsymbol{U}}_{\text{snap}}) + \frac{\gamma}{2}\|\Xi\|_F^2\right]. \tag{24}$$

3.3. Proper orthogonal decomposition-based nonlinear manifolds

There are many different ways to realize a minimization for Eq. (24) in order to obtain $\boldsymbol{\Phi}_{\text{lin}}$, $\bar{\boldsymbol{\Phi}}_{\text{nonlin}}$, and Ξ, such as, by means of POD Geelen et al. (2024), Barnett and Farhat (2022), Geelen et al. (2023a) or data-driven Geelen et al. (2023b,a), Prume et al. (2025), and operator inference Geelen et al. (2023b), Gruber and Tezaur (2023), Gosea et al. (2023) based methods. Here, a classical POD-based nonlinear manifold method is employed for two reasons. On the one hand, this is due to its widespread usage and its stable characteristics, see Ghavamian et al. (2017), Radermacher and Reese (2016), Zhang et al. (2025a). On the other hand, the employment of the POD method leads to a comprehensible expression for the coefficient matrices, avoiding a black-box approximation. In this context, the nodal snapshot matrix $\boldsymbol{U}_{\text{snap}}$ is decomposed via a *thin* singular value decomposition (SVD).

$$\boldsymbol{U}_{\text{snap}} = \boldsymbol{S}\,\boldsymbol{\Sigma}\,\boldsymbol{V}^{\text{T}} \quad \text{with} \quad \boldsymbol{S} = \Big[\underbrace{\boldsymbol{S}_1, \dots \boldsymbol{S}_r}_{\boldsymbol{\Phi}_{\text{lin}}}, \underbrace{\dots \boldsymbol{S}_{r+q}}_{\bar{\boldsymbol{\Phi}}_{\text{nonlin}}}, \dots \boldsymbol{S}_{n_{\text{step}}}\Big] \in \mathbb{R}^{n\times n_{\text{step}}} \tag{25}$$

Here, $\boldsymbol{S}$ denotes the left orthonormal singular basis matrix which contains the left singular vectors. $\boldsymbol{\Sigma}$ represents a diagonal matrix, expressed as $\boldsymbol{\Sigma} = \text{diag}(\sigma_1, \dots, \sigma_{r_a})$, which contains the corresponding singular values in a descending order, i.e., $\sigma_1 > \dots > \sigma_{r_a}$, where $r_a = \text{rank}(\boldsymbol{U}_{\text{snap}})$. The matrix $\boldsymbol{V}^{\text{T}}$ denotes the transposed right orthonormal singular basis matrix with the dimension $\mathbb{R}^{r_a\times r_a}$. By employing a *thin* SVD, the decomposition of the high-dimensional snapshot matrix can be performed more efficiently than with a *full* SVD, since the matrices $\boldsymbol{S}$ and $\boldsymbol{\Sigma}$ are not required to have the full dimensions $\mathbb{R}^{n\times n}$ and $\mathbb{R}^{n\times r_a}$, respectively, where $n \gg r_a$. Subsequently, the linear and nonlinear projection matrices are obtained by truncating $\boldsymbol{S}$ with a user-defined accuracy. Having $\boldsymbol{\Phi}_{\text{lin}}$ and $\bar{\boldsymbol{\Phi}}_{\text{nonlin}}$ at hand, the next step is to determine the coefficient matrix Ξ through the minimization of Eq. (24). In addition, the reduced snapshot matrix is expressed as $\widetilde{\boldsymbol{U}}_{\text{snap}} = \boldsymbol{\Phi}_{\text{lin}}^{\text{T}}\,\boldsymbol{U}_{\text{snap}}$. For brevity, the objective function of the regularized Frobenius norm is defined as $\mathcal{M}$, and it follows:

$$\mathcal{M} = \mathcal{F}(\boldsymbol{\Phi}_{\text{lin}}, \bar{\boldsymbol{\Phi}}_{\text{nonlin}}, \Xi, \widetilde{\boldsymbol{U}}_{\text{snap}}) + \frac{\gamma}{2}\|\Xi\|_F^2 \tag{26a}$$

$$= \frac{1}{2}\|\boldsymbol{U}_{\text{snap}} - \boldsymbol{\Phi}_{\text{lin}}\,\widetilde{\boldsymbol{U}}_{\text{snap}} - \bar{\boldsymbol{\Phi}}_{\text{nonlin}}\,\Xi\,\underbrace{\boldsymbol{g}(\widetilde{\boldsymbol{U}}_{\text{snap}})}_{:=\mathbf{W}}\|_F^2 + \frac{\gamma}{2}\|\Xi\|_F^2 \tag{26b}$$

$$= \frac{1}{2}\left\|\left(\boldsymbol{I}_n - \boldsymbol{\Phi}_{\text{lin}}\,\boldsymbol{\Phi}_{\text{lin}}^{\text{T}}\right)\boldsymbol{U}_{\text{snap}} - \bar{\boldsymbol{\Phi}}_{\text{nonlin}}\,\Xi\,\mathbf{W}\right\|_F^2 + \frac{\gamma}{2}\|\Xi\|_F^2. \tag{26c}$$

The Frobenius norm of an arbitrary matrix $\boldsymbol{X}$ can be calculated as $\|\boldsymbol{X}\|_F^2 := \text{tr}(\boldsymbol{X}^{\text{T}}\boldsymbol{X}) = \sum_{i>n}^{r_{\text{x}}} \sigma_i^2$, where r_{x} is the rank of the matrix $\boldsymbol{X}$ and σ_i is i-th singular value. Hence, using the trace operator tr(•), the regularized Frobenius norm $\mathcal{M}$ in Eq. (26c) can be expressed as:

$$\mathcal{M} = \frac{1}{2}\,\text{tr}\left[\left(\left(\boldsymbol{I}_n - \boldsymbol{\Phi}_{\text{lin}}\,\boldsymbol{\Phi}_{\text{lin}}^{\text{T}}\right)\boldsymbol{U}_{\text{snap}} - \bar{\boldsymbol{\Phi}}_{\text{nonlin}}\,\Xi\,\mathbf{W}\right)^{\text{T}}\left(\left(\boldsymbol{I}_n - \boldsymbol{\Phi}_{\text{lin}}\,\boldsymbol{\Phi}_{\text{lin}}^{\text{T}}\right)\boldsymbol{U}_{\text{snap}} - \bar{\boldsymbol{\Phi}}_{\text{nonlin}}\,\Xi\,\mathbf{W}\right)\right] + \frac{\gamma}{2}\,\text{tr}(\Xi^{\text{T}}\,\Xi). \tag{27}$$

To minimize $\mathcal{M}$, its partial derivative with respect to the coefficient matrix Ξ needs to be computed. With

$$\left(\boldsymbol{I}_n - \boldsymbol{\Phi}_{\text{lin}}\,\boldsymbol{\Phi}_{\text{lin}}^{\text{T}}\right)^{\text{T}} = \boldsymbol{I}_n - \boldsymbol{\Phi}_{\text{lin}}\,\boldsymbol{\Phi}_{\text{lin}}^{\text{T}}, \tag{28}$$

where $\boldsymbol{I}_n \in \mathbb{R}^{n\times n}$ denotes the identity matrix, this leads to

$$\frac{\partial\mathcal{M}}{\partial\Xi} = -\boldsymbol{U}_{\text{snap}}^{\text{T}}\left(\boldsymbol{I}_n - \boldsymbol{\Phi}_{\text{lin}}\,\boldsymbol{\Phi}_{\text{lin}}^{\text{T}}\right)\bar{\boldsymbol{\Phi}}_{\text{nonlin}}\,\mathbf{W} + \mathbf{W}^{\text{T}}\,\Xi^{\text{T}}\,\underbrace{\bar{\boldsymbol{\Phi}}_{\text{nonlin}}^{\text{T}}\,\bar{\boldsymbol{\Phi}}_{\text{nonlin}}}_{\boldsymbol{I}_{(p-1)\,q}}\,\mathbf{W} + \gamma\,\Xi. \tag{29}$$

By setting Eq. (29) to $\mathbf{0}$, the following equation is obtained:

$$\bar{\boldsymbol{\Phi}}_{\text{nonlin}}\left(\boldsymbol{I}_n - \boldsymbol{\Phi}_{\text{lin}}\,\boldsymbol{\Phi}_{\text{lin}}^{\text{T}}\right)\boldsymbol{U}_{\text{snap}}^{\text{T}}\,\mathbf{W} = (\mathbf{W}^{\text{T}}\,\mathbf{W} + \gamma\,\boldsymbol{I}_{(p-1)\,r})\,\Xi. \tag{30a}$$

Due to the convexity of the Frobenius norm Powell (2004), Grussler and Giselsson (2018), the global minimum is guaranteed using Eq. (29). Finally, the coefficient matrix Ξ is obtained as:

$$\Xi = \bar{\boldsymbol{\Phi}}_{\text{nonlin}}^{\text{T}}\left(\boldsymbol{I}_n - \boldsymbol{\Phi}_{\text{lin}}\,\boldsymbol{\Phi}_{\text{lin}}^{\text{T}}\right)\boldsymbol{U}_{\text{snap}}\,\mathbf{W}^{\text{T}}\left(\mathbf{W}\,\mathbf{W}^{\text{T}} + \gamma\,\boldsymbol{I}_{(p-1)\,r}\right)^{-1}. \tag{31}$$

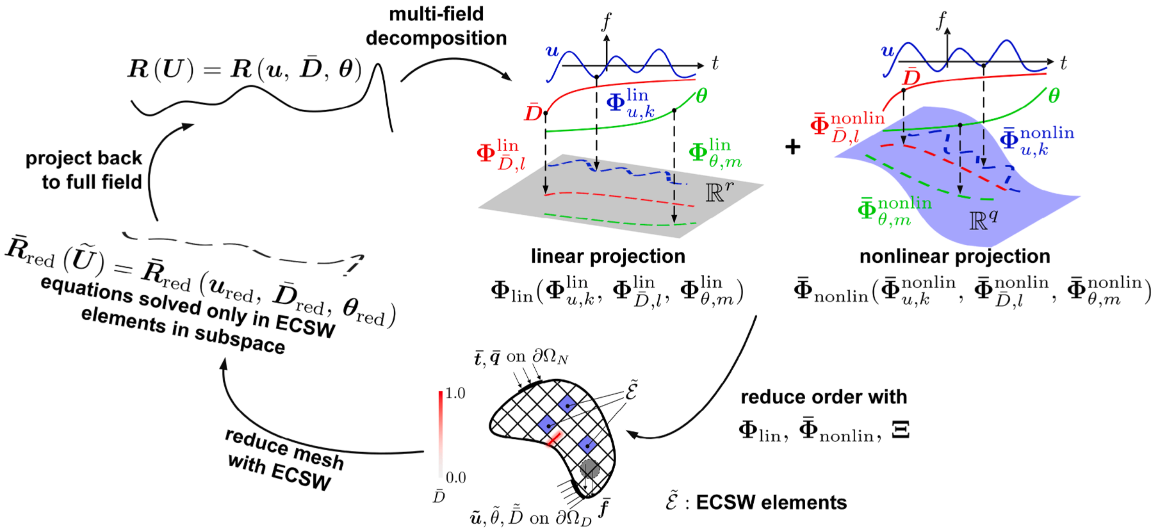

Fig. 1. Schematic illustration of the multi-field decomposed nonlinear manifold MOR process and its corresponding projections. The solid and dashed lines represent the functions of the full-order model (full space) and the reduced-order model (reduced subspace), respectively. The full-order residual vector $\boldsymbol{R}$ is decomposed and projected onto both linear and nonlinear subspaces. $\boldsymbol{\Phi}_{\text{lin}}$ denotes the linear projection matrix which comprises individual projection matrices $\boldsymbol{\Phi}^{\text{lin}}_{u,k}$, $\boldsymbol{\Phi}^{\text{lin}}_{\bar{D},l}$, and $\boldsymbol{\Phi}^{\text{lin}}_{\theta,m}$ for the displacement, nonlocal damage, and temperature fields, respectively. $\bar{\boldsymbol{\Phi}}_{\text{nonlin}}$ represents the nonlinear projection that corresponds to the nonlinear terms. $\bar{\boldsymbol{R}}_{\text{red}}$ denotes the reduced residual vector for the ECSW selected elements $\widetilde{\mathcal{E}}$ (see Section 3.6) in terms of the reduced quantities $\boldsymbol{u}_{\text{red}}$, $\bar{\boldsymbol{D}}_{\text{red}}$, and $\boldsymbol{\theta}_{\text{red}}$.

3.4. Multi-field decomposed nonlinear manifold reduction

The key point of the multi-field decomposed MOR approach is to decompose the nodal solution vector into three individual fields, see Eq. (32), namely the displacement field $\boldsymbol{u}_u$, damage field $\boldsymbol{u}_{\bar{D}}$, and temperature field $\boldsymbol{u}_\theta$. The motivation for additively decomposing the full field into multiple individual fields is the strong nonlinearity of the formulation and its impact on developing a suitable reduced-order model, see Eqs. (2), (A.3), and (A.7). For reduced-order modeling, it is challenging to capture the softening behavior in low-dimensional subspaces using a single-field projection-based method. This problem was also observed by Kerfriden et al. (2011, 2013), Selvaraj and Hallett (2024), Mishra et al. (2024), and Zhang et al. (2025a). To overcome this problem, the multi-field decomposed MOR approach is employed (see Zhang et al. (2025a)) by splitting the solution vector associated with a single node as follows:

$$\boldsymbol{u} = \begin{pmatrix} u \\ v \\ w \\ \bar{D} \\ \theta \end{pmatrix} = \underbrace{\begin{pmatrix} u \\ v \\ w \\ 0 \\ 0 \end{pmatrix}}_{\boldsymbol{u}_u} + \underbrace{\begin{pmatrix} 0 \\ 0 \\ 0 \\ \bar{D} \\ 0 \end{pmatrix}}_{\boldsymbol{u}_{\bar{D}}} + \underbrace{\begin{pmatrix} 0 \\ 0 \\ 0 \\ 0 \\ \theta \end{pmatrix}}_{\boldsymbol{u}_\theta}. \tag{32}$$

The objective of the multi-field decomposed nonlinear manifold MOR is to seek the low-dimensional orthonormal linear projection matrix $\boldsymbol{\Phi}_{\text{lin}} \in \mathbb{R}^{n\times r}$ and nonlinear projection matrix $\bar{\boldsymbol{\Phi}}_{\text{nonlin}} \in \mathbb{R}^{n\times q}$, which project the global residual vector $\boldsymbol{R}$ and stiffness matrix $\boldsymbol{K}$ onto reduced subspaces, as defined in Eq. (17) and schematically illustrated in Fig. 1. These projections are realized not only in a linear and nonlinear manner but also individually for the displacement, nonlocal damage, and temperature fields.

Hence, the global solution vector is decomposed into a displacement field $\boldsymbol{U}_u = [\boldsymbol{u}_u^1, \boldsymbol{u}_u^2, \dots \boldsymbol{u}_u^\lambda]^{\text{T}}$, a nonlocal damage field $\boldsymbol{U}_{\bar{D}} = [\boldsymbol{u}_{\bar{D}}^1, \boldsymbol{u}_{\bar{D}}^2, \dots \boldsymbol{u}_{\bar{D}}^\lambda]^{\text{T}}$, and a temperature field $\boldsymbol{U}_\theta = [\boldsymbol{u}_\theta^1, \boldsymbol{u}_\theta^2, \dots \boldsymbol{u}_\theta^\lambda]^{\text{T}}$, respectively. Here, the symbol λ denotes the total number of nodes in the unreduced discretization $\mathcal{E}$. The decomposition of the solution vector of a single node $\boldsymbol{u}$, as presented in Eq. (32), enables the decoupling of distinct field quantities, thereby allowing separate projection operations for each component. From an implementation perspective, filling the corresponding vectors with zeros ensures consistency in the dimensions of vectors and matrices associated with different field quantities within the reduced-order modeling framework Zhang et al. (2025a). As a result, decomposed snapshots are defined as $\boldsymbol{U}^u_{\text{snap}}$, $\boldsymbol{U}^{\bar{D}}_{\text{snap}}$, and $\boldsymbol{U}^\theta_{\text{snap}}$ corresponding to the displacement, nonlocal damage, and temperature fields as:

$$\boldsymbol{U}^u_{\text{snap}} = \left[\boldsymbol{U}^1_u, \dots, \boldsymbol{U}^k_u, \dots \boldsymbol{U}^{n_{\text{step}}}_u\right], \quad \boldsymbol{U}^{\bar{D}}_{\text{snap}} = \left[\boldsymbol{U}^1_{\bar{D}}, \dots, \boldsymbol{U}^l_{\bar{D}}, \dots \boldsymbol{U}^{n_{\text{step}}}_{\bar{D}}\right], \quad \boldsymbol{U}^\theta_{\text{snap}} = \left[\boldsymbol{U}^1_\theta, \dots, \boldsymbol{U}^m_\theta, \dots \boldsymbol{U}^{n_{\text{step}}}_\theta\right]. \tag{33}$$

The indices k, l, and m denote independently selected truncation numbers corresponding to the number of displacement, nonlocal damage, and temperature modes, respectively, thereby defining the dimensions of the projection matrices for each field. By employing a *thin* singular value decomposition $\mathbf{SVD}(\bullet)$ for the different snapshot matrices, one obtains:

$$\left\{\boldsymbol{S}_u, \boldsymbol{\Sigma}_u, \boldsymbol{V}_u^{\mathrm{T}}\right\} = \mathbf{SVD}(\boldsymbol{U}^u_{\mathrm{snap}}), \quad \left\{\boldsymbol{S}_{\bar{D}}, \boldsymbol{\Sigma}_{\bar{D}}, \boldsymbol{V}_{\bar{D}}^{\mathrm{T}}\right\} = \mathbf{SVD}(\boldsymbol{U}^{\bar{D}}_{\mathrm{snap}}), \quad \left\{\boldsymbol{S}_\theta, \boldsymbol{\Sigma}_\theta, \boldsymbol{V}_\theta^{\mathrm{T}}\right\} = \mathbf{SVD}(\boldsymbol{U}^\theta_{\mathrm{snap}}). \tag{34}$$

Subsequently, the projection matrices of the displacement field $\boldsymbol{\Phi}^{\mathrm{lin}}_{u,k}$, nonlocal damage field $\boldsymbol{\Phi}^{\mathrm{lin}}_{\bar{D},l}$, and temperature field $\boldsymbol{\Phi}^{\mathrm{lin}}_{\theta,m}$ are computed by truncating $\boldsymbol{S}_u$, $\boldsymbol{S}_{\bar{D}}$, and $\boldsymbol{S}_\theta$ at k, l, and m, respectively:

$$\begin{aligned}
&\boldsymbol{S}_u = \Big[\underbrace{\boldsymbol{S}_u^1, \cdots \boldsymbol{S}_u^k}_{\boldsymbol{\Phi}^{\mathrm{lin}}_{u,k}}, \underbrace{\cdots \boldsymbol{S}_u^{k+q}}_{\bar{\boldsymbol{\Phi}}^{\mathrm{nonlin}}_{u,k}}, \cdots \boldsymbol{S}_u^{n_{\mathrm{step}}}\Big], \quad \boldsymbol{S}_{\bar{D}} = \Big[\underbrace{\boldsymbol{S}_{\bar{D}}^1, \cdots \boldsymbol{S}_{\bar{D}}^l}_{\boldsymbol{\Phi}^{\mathrm{lin}}_{\bar{D},l}}, \underbrace{\cdots \boldsymbol{S}_{\bar{D}}^{l+q}}_{\bar{\boldsymbol{\Phi}}^{\mathrm{nonlin}}_{\bar{D},l}}, \cdots \boldsymbol{S}_{\bar{D}}^{n_{\mathrm{step}}}\Big], \\
&\boldsymbol{S}_\theta = \Big[\underbrace{\boldsymbol{S}_\theta^1, \cdots \boldsymbol{S}_\theta^m}_{\boldsymbol{\Phi}^{\mathrm{lin}}_{\theta,m}}, \underbrace{\cdots \boldsymbol{S}_\theta^{m+q}}_{\bar{\boldsymbol{\Phi}}^{\mathrm{nonlin}}_{\theta,m}}, \cdots \boldsymbol{S}_\theta^{n_{\mathrm{step}}}\Big].
\end{aligned} \tag{35}$$

The nonlinear components $\bar{\boldsymbol{\Phi}}^{\mathrm{nonlin}}_{u,k}$, $\bar{\boldsymbol{\Phi}}^{\mathrm{nonlin}}_{\bar{D},l}$, and $\bar{\boldsymbol{\Phi}}^{\mathrm{nonlin}}_{\theta,m}$ are obtained as expressed in Eq. (35). For simplicity and consistency, the number of nonlinear modes is uniformly selected as q across the different physical fields. A similar strategy for constructing the nonlinear projection basis has been adopted in prior studies Cohen et al. (2023), Geelen et al. (2024, 2023a). Consequently, the global linear projection matrix $\boldsymbol{\Phi}_{\mathrm{lin}} \in \mathbb{R}^{n\times r}$ and the global nonlinear projection matrix $\bar{\boldsymbol{\Phi}}_{\mathrm{nonlin}} \in \mathbb{R}^{n\times 3q}$ are obtained using the mode numbers k, l, and m associated with the three respective fields as:

$$\boldsymbol{\Phi}_{\mathrm{lin}} = \left[\boldsymbol{\Phi}^{\mathrm{lin}}_{u,k}, \boldsymbol{\Phi}^{\mathrm{lin}}_{\bar{D},l}, \boldsymbol{\Phi}^{\mathrm{lin}}_{\theta,m}\right], \quad \bar{\boldsymbol{\Phi}}_{\mathrm{nonlin}} = \left[\bar{\boldsymbol{\Phi}}^{\mathrm{nonlin}}_{u,k}, \bar{\boldsymbol{\Phi}}^{\mathrm{nonlin}}_{\bar{D},l}, \bar{\boldsymbol{\Phi}}^{\mathrm{nonlin}}_{\theta,m}\right]. \tag{36}$$

To ensure a sufficient reduction, the total number of linear r and nonlinear q modes should satisfy $r \ll n$ and $q \ll n$, where $r = k + l + m$. Corresponding to the multi-field decomposed linear and nonlinear projection matrices, the decomposed coefficient matrices for the displacement, nonlocal damage, and temperature fields are denoted as $\boldsymbol{\Xi}_u$, $\boldsymbol{\Xi}_{\bar{D}}$, and $\boldsymbol{\Xi}_\theta$, respectively. Accordingly, the objective function is expressed in terms of additional penalty parameters γ_u, $\gamma_{\bar{D}}$, and γ_θ applied to the corresponding fields as follows:

$$\boldsymbol{\Xi} = \underset{\{\boldsymbol{\Xi}_u, \boldsymbol{\Xi}_{\bar{D}}, \boldsymbol{\Xi}_\theta\}}{\arg\min} \left[\mathcal{F}\,(\boldsymbol{\Phi}_{\mathrm{lin}}, \bar{\boldsymbol{\Phi}}_{\mathrm{nonlin}}, \boldsymbol{\Xi}, \widetilde{\boldsymbol{U}}_{\mathrm{snap}}) + \frac{\gamma_u}{2}\|\boldsymbol{\Xi}_u\|_F^2 + \frac{\gamma_{\bar{D}}}{2}\|\boldsymbol{\Xi}_{\bar{D}}\|_F^2 + \frac{\gamma_\theta}{2}\|\boldsymbol{\Xi}_\theta\|_F^2\right]. \tag{37}$$

Here, the global coefficient matrix $\boldsymbol{\Xi} \in \mathbb{R}^{3q\times(p-1)r}$ is expressed as a block diagonal matrix composed of the contributions from different fields as:

$$\boldsymbol{\Xi} = \begin{pmatrix} \boldsymbol{\Xi}_u & \mathbf{0} & \mathbf{0} \\ \mathbf{0} & \boldsymbol{\Xi}_{\bar{D}} & \mathbf{0} \\ \mathbf{0} & \mathbf{0} & \boldsymbol{\Xi}_\theta \end{pmatrix}. \tag{38}$$

By decomposing Eq. (37) into three individual fields corresponding to displacement, nonlocal damage, and temperature, the associated objective function for minimization is expressed as:

$$\begin{aligned}
\boldsymbol{\Xi} = \underset{\{\boldsymbol{\Xi}_u, \boldsymbol{\Xi}_{\bar{D}}, \boldsymbol{\Xi}_\theta\}}{\arg\min} \Big[&\underbrace{\mathcal{F}_u\,(\boldsymbol{\Phi}^{\mathrm{lin}}_{u,k}, \bar{\boldsymbol{\Phi}}^{\mathrm{nonlin}}_{u,k}, \boldsymbol{\Xi}_u, \widetilde{\boldsymbol{U}}^u_{\mathrm{snap}}) + \frac{\gamma_u}{2}\,\|\boldsymbol{\Xi}_u\|_F^2}_{\text{displacement field}} + \underbrace{\mathcal{F}_{\bar{D}}\,(\boldsymbol{\Phi}^{\mathrm{lin}}_{\bar{D},l}, \bar{\boldsymbol{\Phi}}^{\mathrm{nonlin}}_{\bar{D},k}, \boldsymbol{\Xi}_{\bar{D}}, \widetilde{\boldsymbol{U}}^{\bar{D}}_{\mathrm{snap}}) + \frac{\gamma_{\bar{D}}}{2}\,\|\boldsymbol{\Xi}_{\bar{D}}\|_F^2}_{\text{nonlocal damage field}} \\
&\underbrace{+\,\mathcal{F}_\theta\,(\boldsymbol{\Phi}^{\mathrm{lin}}_{\theta,k}, \bar{\boldsymbol{\Phi}}^{\mathrm{nonlin}}_{\theta,k}, \boldsymbol{\Xi}_\theta, \widetilde{\boldsymbol{U}}^\theta_{\mathrm{snap}}) + \frac{\gamma_\theta}{2}\,\|\boldsymbol{\Xi}_\theta\|_F^2}_{\text{temperature field}}\Big].
\end{aligned} \tag{39}$$

Compared with the merged minimization approach presented in Geelen et al. (2023a,b, 2024), a scaling issue can arise particularly in the case of multiphysics problems, as noted in Washabaugh (2016), Lindsay et al. (2022), Parish and Rizzi (2023). To address this issue and build upon prior work on multi-field decomposed reduced-order modeling Zhang et al. (2025a), the objective function in Eq. (24) is newly decomposed into three separate fields, as shown in Eqs. (37) and (39). This strategy enhances the reduction performance since the coefficient matrices can be individually tuned for the displacement, nonlocal damage, and temperature fields. Accordingly, these matrices can be similarly derived as in Eq. (31):

$$\boldsymbol{\Xi}_u = (\bar{\boldsymbol{\Phi}}^{\mathrm{nonlin}}_{u,k})^{\mathrm{T}}\left(\boldsymbol{I}_n - \boldsymbol{\Phi}^{\mathrm{lin}}_{u,k}\left(\boldsymbol{\Phi}^{\mathrm{lin}}_{u,k}\right)^{\mathrm{T}}\right)\boldsymbol{U}^u_{\mathrm{snap}}\,\mathbf{W}_u^{\mathrm{T}}\left(\mathbf{W}_u\,\mathbf{W}_u^{\mathrm{T}} + \gamma_u\,\boldsymbol{I}_{(p-1)\,k}\right)^{-1}, \tag{40a}$$

$$\boldsymbol{\Xi}_{\bar{D}} = (\bar{\boldsymbol{\Phi}}^{\mathrm{nonlin}}_{\bar{D},l})^{\mathrm{T}}\left(\boldsymbol{I}_n - \boldsymbol{\Phi}^{\mathrm{lin}}_{\bar{D},l}\,(\boldsymbol{\Phi}^{\mathrm{lin}}_{\bar{D},l})^{\mathrm{T}}\right)\boldsymbol{U}^{\bar{D}}_{\mathrm{snap}}\,\mathbf{W}_{\bar{D}}^{\mathrm{T}}\left(\mathbf{W}_{\bar{D}}\,\mathbf{W}_{\bar{D}}^{\mathrm{T}} + \gamma_{\bar{D}}\,\boldsymbol{I}_{(p-1)\,l}\right)^{-1}, \tag{40b}$$

$$\boldsymbol{\Xi}_\theta = (\bar{\boldsymbol{\Phi}}^{\mathrm{nonlin}}_{\theta,m})^{\mathrm{T}}\left(\boldsymbol{I}_n - \boldsymbol{\Phi}^{\mathrm{lin}}_{\theta,m}\,(\boldsymbol{\Phi}^{\mathrm{lin}}_{\theta,m})^{\mathrm{T}}\right)\boldsymbol{U}^\theta_{\mathrm{snap}}\,\mathbf{W}_\theta^{\mathrm{T}}\left(\mathbf{W}_\theta\,\mathbf{W}_\theta^{\mathrm{T}} + \gamma_\theta\,\boldsymbol{I}_{(p-1)\,m}\right)^{-1}. \tag{40c}$$

3.5. Multi-state and multi-field decomposed nonlinear manifold MOR for prediction

To assess the predictive performance of the proposed MOR approach in the numerical examples later on, the *predictive* linear and nonlinear projection matrices $\boldsymbol{\Phi}^{\mathrm{pred}}_{\mathrm{lin}}$ and $\bar{\boldsymbol{\Phi}}^{\mathrm{pred}}_{\mathrm{nonlin}}$ are constructed using the multi-field and multi-state decomposition method, see Fig. 2. Concretely speaking, these matrices are built by taking into account additional snapshots from full-order simulations.

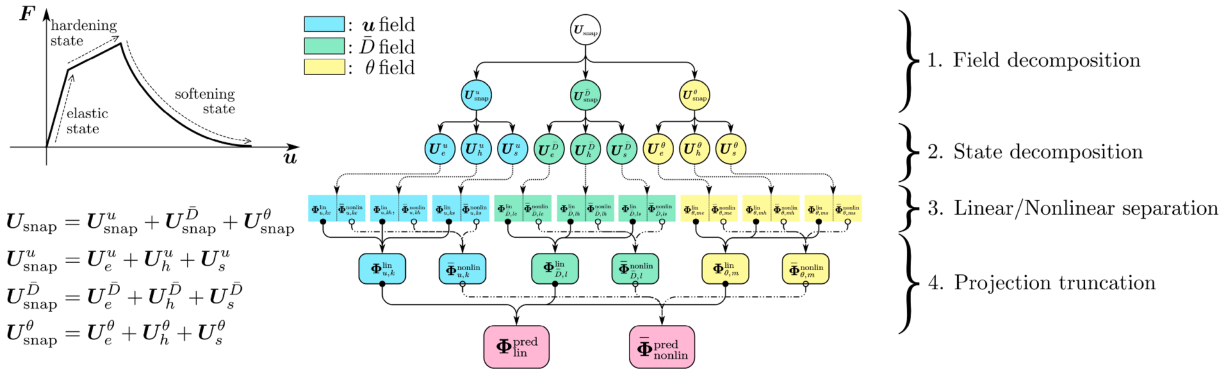

Fig. 2. Schematic illustration of the multi-field and multi-state decomposed nonlinear manifold MOR process proposed in this work and the corresponding projections.

These simulations are conducted with deviations in the elastic parameters μ and Λ of $\pm d\%$, where d is a chosen value. Importantly, only half of the snapshots are collected to maintain dimensional consistency with Eq. (33) in terms of the number of snapshots. The resulting decomposed snapshots for a positive deviation ($+d\%$) are separated into displacement, nonlocal damage, and temperature fields according to:

$$\boldsymbol{U}^{u}_{\text{snap},+d} = \left[\boldsymbol{U}^{1}_{u}, \boldsymbol{U}^{3}_{u}, \dots, \boldsymbol{U}^{n_{\text{step}}-1}_{u}\right], \quad \boldsymbol{U}^{\bar{D}}_{\text{snap},+d} = \left[\boldsymbol{U}^{1}_{\bar{D}}, \boldsymbol{U}^{3}_{\bar{D}}, \dots, \boldsymbol{U}^{n_{\text{step}}-1}_{\bar{D}}\right], \quad \boldsymbol{U}^{\theta}_{\text{snap},+d} = \left[\boldsymbol{U}^{1}_{\theta}, \boldsymbol{U}^{3}_{\theta}, \dots, \boldsymbol{U}^{n_{\text{step}}-1}_{\theta}\right]. \tag{41}$$

The snapshots for the negative deviation ($-d\%$) are obtained analogously to Eq. (41) as $\boldsymbol{U}^{u}_{\text{snap},-d}$, $\boldsymbol{U}^{\bar{D}}_{\text{snap},-d}$, and $\boldsymbol{U}^{\theta}_{\text{snap},-d}$, respectively. The combined snapshots are then expressed as:

$$\boldsymbol{U}^{u}_{\text{snap, pred}} = \left[\boldsymbol{U}^{u}_{\text{snap},-d}; \boldsymbol{U}^{u}_{\text{snap},+d}\right], \quad \boldsymbol{U}^{\bar{D}}_{\text{snap, pred}} = \left[\boldsymbol{U}^{\bar{D}}_{\text{snap},-d}; \boldsymbol{U}^{\bar{D}}_{\text{snap},+d}\right], \quad \boldsymbol{U}^{\theta}_{\text{snap, pred}} = \left[\boldsymbol{U}^{\theta}_{\text{snap},-d}; \boldsymbol{U}^{\theta}_{\text{snap},+d}\right]. \tag{42}$$

By employing Eqs. (34), (35), and (36), the *predictive* projection matrices $\boldsymbol{\Phi}^{\text{pred}}_{\text{lin}}$ and $\bar{\boldsymbol{\Phi}}^{\text{pred}}_{\text{nonlin}}$ are evaluated and later used to predict the thermo-mechanical response within the material parameter intervals $[(1-d\%)\,\mu, (1+d\%)\,\mu]$ and $[(1-d\%)\,\Lambda, (1+d\%)\,\Lambda]$.
As a result, the final global snapshot matrix $\boldsymbol{U}_{\text{snap}}$, which consists of the decomposed snapshots of three fields, is given as follows:

$$\boldsymbol{U}_{\text{snap}} = \boldsymbol{U}^{u}_{\text{snap}} + \boldsymbol{U}^{\bar{D}}_{\text{snap}} + \boldsymbol{U}^{\theta}_{\text{snap}}, \tag{43a}$$

$$\boldsymbol{U}^{u}_{\text{snap}} = \boldsymbol{U}^{u}_{e} + \boldsymbol{U}^{u}_{h} + \boldsymbol{U}^{u}_{s}, \quad \boldsymbol{U}^{\bar{D}}_{\text{snap}} = \boldsymbol{U}^{\bar{D}}_{e} + \boldsymbol{U}^{\bar{D}}_{h} + \boldsymbol{U}^{\bar{D}}_{s}, \quad \boldsymbol{U}^{\theta}_{\text{snap}} = \boldsymbol{U}^{\theta}_{e} + \boldsymbol{U}^{\theta}_{h} + \boldsymbol{U}^{\theta}_{s}. \tag{43b}$$

To accurately select the number of modes, a multi-state decomposed approach inspired by Oliver et al. (2017) is newly proposed in this study, in which the displacement field snapshots are additionally decomposed into three distinct mechanical states: state in the elastic regime $\boldsymbol{U}^{u}_{e}$, state where plastic hardening takes place $\boldsymbol{U}^{u}_{h}$, and state where softening occurs $\boldsymbol{U}^{u}_{s}$, see Fig. 2. Based on this multi-state decomposition, the snapshots of the displacement field are separated as follows:

$$\underbrace{\begin{pmatrix} \boldsymbol{U}^{1}_{u} \\ \vdots \\ \boldsymbol{U}^{n_e}_{u} \\ \vdots \\ \boldsymbol{U}^{n_h}_{u} \\ \vdots \\ \boldsymbol{U}^{n_{\text{step}}}_{u} \end{pmatrix}}_{\boldsymbol{U}^{u}_{\text{snap}}} = \underbrace{\begin{pmatrix} \boldsymbol{U}^{1}_{u} \\ \vdots \\ \boldsymbol{U}^{n_e}_{u} \\ \vdots \\ \boldsymbol{0} \\ \vdots \\ \boldsymbol{0} \end{pmatrix}}_{\boldsymbol{U}^{u}_{e}} + \underbrace{\begin{pmatrix} \boldsymbol{0} \\ \vdots \\ \boldsymbol{U}^{n_e+1}_{u} \\ \vdots \\ \boldsymbol{U}^{n_h}_{u} \\ \vdots \\ \boldsymbol{0} \end{pmatrix}}_{\boldsymbol{U}^{u}_{h}} + \underbrace{\begin{pmatrix} \boldsymbol{0} \\ \vdots \\ \boldsymbol{0} \\ \vdots \\ \boldsymbol{U}^{n_h+1}_{u} \\ \vdots \\ \boldsymbol{U}^{n_{\text{step}}}_{u} \end{pmatrix}}_{\boldsymbol{U}^{u}_{s}}. \tag{44}$$

Here, n_e and n_h denote the step number at the end of the elastic state and the hardening state, respectively. Subsequently, individual *thin* singular value decompositions are applied to different displacement field snapshot states:

$$\boldsymbol{U}^{u}_{e} = \boldsymbol{S}^{u}_{e}\boldsymbol{\Sigma}^{u}_{e}\boldsymbol{V}^{u\text{T}}_{e}, \quad \boldsymbol{U}^{u}_{h} = \boldsymbol{S}^{u}_{h}\boldsymbol{\Sigma}^{u}_{h}\boldsymbol{V}^{u\text{T}}_{h}, \quad \boldsymbol{U}^{u}_{s} = \boldsymbol{S}^{u}_{s}\boldsymbol{\Sigma}^{u}_{s}\boldsymbol{V}^{u\text{T}}_{s}, \quad \text{and} \quad \boldsymbol{U}^{u}_{\text{snap}} = \boldsymbol{S}^{u}\boldsymbol{\Sigma}^{u}\boldsymbol{V}^{u\text{T}}. \tag{45}$$

For snapshots in the displacement field, the following relation can hold

$$\boldsymbol{U}^{u}_{e} + \boldsymbol{U}^{u}_{h} + \boldsymbol{U}^{u}_{s} \quad \Rightarrow \quad \boldsymbol{S}^{u}_{ehs} = \left[\boldsymbol{S}^{u}_{e} \quad \boldsymbol{S}^{u}_{h} \quad \boldsymbol{S}^{u}_{s}\right] \in \mathbb{R}^{n \times n_{\text{step}}}. \tag{46}$$

Eq. (46) defines the merged projection matrix $\boldsymbol{S}^{u}_{ehs}$ for the displacement field, constructed from the multi-state decomposed snapshots corresponding to the elastic, hardening, and softening regions. However, this merged basis does not satisfy $\boldsymbol{S}^{u}_{ehs} = \boldsymbol{S}_{u}$ and cannot directly replace $\boldsymbol{S}_{u}$ in Eq. (34) for approximating the full-order displacement field. This is because simply concatenating the projection matrices $\boldsymbol{S}^{u}_{e}$, $\boldsymbol{S}^{u}_{h}$, and $\boldsymbol{S}^{u}_{s}$, derived from different mechanical states, does not ensure mutual orthogonality among the resulting basis vectors. Thus, a randomized singular value decomposition (rSVD) Woolfe et al. (2008), Liberty et al. (2007), Halko et al. (2011), Rokhlin et al. (2010) is applied to the combined bases. This approach not only preserves orthogonality across different physical states in reduced-order simulations but also enables precise control over the number of modes. More concretely, the merged subspaces are projected onto a lower-dimensional space via the multiplication with a Gaussian random matrix $\boldsymbol{\Omega} \in \mathbb{R}^{(r_e+r_h+r_s)\times\kappa}$, where κ denotes the target rank of the reduced subspace. Specifically, the random projection is expressed as $\boldsymbol{\Omega} \sim \mathcal{N}(0,1)$, $\boldsymbol{Y}_u = \boldsymbol{S}^u_{ehs}\,\boldsymbol{\Omega} \in \mathbb{R}^{n\times\kappa}$. This intermediate matrix $\boldsymbol{Y}_u$ is essential in capturing the dominant features of the combined bases $\boldsymbol{S}^u_e$, $\boldsymbol{S}^u_h$, and $\boldsymbol{S}^u_s$. An orthonormal approximation of the left singular vectors is then obtained by applying a QR decomposition Gander (1980), Goodall (1993) to $\boldsymbol{Y}_u$, yielding

$$\{\boldsymbol{Q}, \boldsymbol{\mathcal{R}}\} = \mathcal{QR}\,(\boldsymbol{Y}_u), \tag{47}$$

where $\boldsymbol{Q} \in \mathbb{R}^{n\times\kappa}$ is orthonormal and captures the main directions of the combined subspace, and $\boldsymbol{\mathcal{R}} \in \mathbb{R}^{\kappa\times\kappa}$ denotes an upper triangular matrix ($\mathcal{R}_{ij} = 0,\ i > j$). Here, $\mathcal{QR}(\bullet)$ denotes the operator for the QR decomposition. To combine the contributions of $\boldsymbol{S}^u_e$, $\boldsymbol{S}^u_h$, and $\boldsymbol{S}^u_s$, they are projected onto the subspace spanned by $\boldsymbol{Q}$. This process ensures that the combined information from $\boldsymbol{S}^u_e$, $\boldsymbol{S}^u_h$, and $\boldsymbol{S}^u_s$ is accurately reflected in $\boldsymbol{S}_u$. This is achieved by projecting each matrix as follows:

$$\widetilde{\boldsymbol{S}}^u_e = \boldsymbol{Q}^{\mathrm{T}}\boldsymbol{S}^u_e, \quad \widetilde{\boldsymbol{S}}^u_h = \boldsymbol{Q}^{\mathrm{T}}\boldsymbol{S}^u_h, \quad \widetilde{\boldsymbol{S}}^u_s = \boldsymbol{Q}^{\mathrm{T}}\boldsymbol{S}^u_s. \tag{48}$$

The projections $\widetilde{\boldsymbol{S}}^u_e$, $\widetilde{\boldsymbol{S}}^u_h$, and $\widetilde{\boldsymbol{S}}^u_s$ capture the contributions of the left singular matrices of $\boldsymbol{U}^u_e$, $\boldsymbol{U}^u_h$, and $\boldsymbol{U}^u_s$, respectively, to the subspace defined by $\boldsymbol{Q}$. These projected components are subsequently combined to construct a unified multi-state projection $\boldsymbol{S}^u_{ehs}$ in the displacement field. As the projections in Eq. (48) are expressed within the subspace spanned by $\boldsymbol{Q}$, they are concatenated as follows:

$$\boldsymbol{S}^u_{ehs} = \boldsymbol{Q}\left[\boldsymbol{Q}^{\mathrm{T}}\boldsymbol{S}^u_e \quad \boldsymbol{Q}^{\mathrm{T}}\boldsymbol{S}^u_h \quad \boldsymbol{Q}^{\mathrm{T}}\boldsymbol{S}^u_s\right] \quad \Rightarrow \quad \boldsymbol{S}^u_{ehs} \approx \boldsymbol{S}_u. \tag{49}$$

Having those consistent left singular matrices at hand, the global projection matrix in the displacement field over multiple states is obtained by truncating the left singular matrices $\boldsymbol{H}^u_e = \boldsymbol{Q}\,(\boldsymbol{Q}^{\mathrm{T}}\boldsymbol{S}^u_e)$, $\boldsymbol{H}^u_h = \boldsymbol{Q}\,(\boldsymbol{Q}^{\mathrm{T}}\boldsymbol{S}^u_h)$, and $\boldsymbol{H}^u_s = \boldsymbol{Q}\,(\boldsymbol{Q}^{\mathrm{T}}\boldsymbol{S}^u_s)$ with the number of selected modes k_e, k_h, and k_s, respectively:

$$\begin{aligned}
\boldsymbol{H}^u_e &= \Big[\underbrace{\boldsymbol{H}^{u,1}_e, \cdots \boldsymbol{H}^{u,i}_e}_{\boldsymbol{\Phi}^{\mathrm{lin}}_{u,k_e}}, \underbrace{\cdots\ \boldsymbol{H}^{u,j}_e}_{\bar{\boldsymbol{\Phi}}^{\mathrm{nonlin}}_{u,k_e}}, \cdots\ \boldsymbol{H}^{u,r}_e\Big], \qquad \boldsymbol{H}^u_h = \Big[\underbrace{\boldsymbol{H}^{u,1}_h, \cdots \boldsymbol{H}^{u,i}_h}_{\boldsymbol{\Phi}^{\mathrm{lin}}_{u,k_h}}, \underbrace{\cdots\ \boldsymbol{H}^{u,j}_h}_{\bar{\boldsymbol{\Phi}}^{\mathrm{nonlin}}_{u,k_h}}, \cdots\ \boldsymbol{H}^{u,r}_h\Big], \\
\boldsymbol{H}^u_s &= \Big[\underbrace{\boldsymbol{H}^{u,1}_s, \cdots \boldsymbol{H}^{u,i}_s}_{\boldsymbol{\Phi}^{\mathrm{lin}}_{u,k_s}}, \underbrace{\cdots\ \boldsymbol{H}^{u,j}_s}_{\bar{\boldsymbol{\Phi}}^{\mathrm{nonlin}}_{u,k_s}}, \cdots\ \boldsymbol{H}^{u,r}_s\Big].
\end{aligned} \tag{50}$$

Analogously, following Eqs. (48), (49), and (50), one can obtain the predictive linear and nonlinear global projection matrices over different fields as $\boldsymbol{\Phi}_{\mathrm{lin}} = \boldsymbol{\Phi}^{\mathrm{pred}}_{\mathrm{lin}}$ and $\bar{\boldsymbol{\Phi}}_{\mathrm{nonlin}} = \bar{\boldsymbol{\Phi}}^{\mathrm{pred}}_{\mathrm{nonlin}}$:

$$\boldsymbol{\Phi}^{\mathrm{pred}}_{\mathrm{lin}} = \Big[\underbrace{\boldsymbol{\Phi}^{\mathrm{lin}}_{u,k_e}, \boldsymbol{\Phi}^{\mathrm{lin}}_{u,k_h}, \boldsymbol{\Phi}^{\mathrm{lin}}_{u,k_s}}_{\boldsymbol{\Phi}^{\mathrm{lin}}_{u}}, \underbrace{\boldsymbol{\Phi}^{\mathrm{lin}}_{\bar{D},l_e}, \boldsymbol{\Phi}^{\mathrm{lin}}_{\bar{D},l_h}, \boldsymbol{\Phi}^{\mathrm{lin}}_{\bar{D},l_s}}_{\boldsymbol{\Phi}^{\mathrm{lin}}_{\bar{D}}}, \underbrace{\boldsymbol{\Phi}^{\mathrm{lin}}_{\theta,m_e}, \boldsymbol{\Phi}^{\mathrm{lin}}_{\theta,m_h}, \boldsymbol{\Phi}^{\mathrm{lin}}_{\theta,m_s}}_{\boldsymbol{\Phi}^{\mathrm{lin}}_{\theta}}\Big], \tag{51a}$$

$$\bar{\boldsymbol{\Phi}}^{\mathrm{pred}}_{\mathrm{nonlin}} = \Big[\underbrace{\bar{\boldsymbol{\Phi}}^{\mathrm{nonlin}}_{u,k_e}, \bar{\boldsymbol{\Phi}}^{\mathrm{nonlin}}_{u,k_h}, \bar{\boldsymbol{\Phi}}^{\mathrm{nonlin}}_{u,k_s}}_{\bar{\boldsymbol{\Phi}}^{\mathrm{nonlin}}_{u}}, \underbrace{\bar{\boldsymbol{\Phi}}^{\mathrm{nonlin}}_{\bar{D},l_e}, \bar{\boldsymbol{\Phi}}^{\mathrm{nonlin}}_{\bar{D},l_h}, \bar{\boldsymbol{\Phi}}^{\mathrm{nonlin}}_{\bar{D},l_s}}_{\bar{\boldsymbol{\Phi}}^{\mathrm{nonlin}}_{\bar{D}}}, \underbrace{\bar{\boldsymbol{\Phi}}^{\mathrm{nonlin}}_{\theta,m_e}, \bar{\boldsymbol{\Phi}}^{\mathrm{nonlin}}_{\theta,m_h}, \bar{\boldsymbol{\Phi}}^{\mathrm{nonlin}}_{\theta,m_s}}_{\bar{\boldsymbol{\Phi}}^{\mathrm{nonlin}}_{\theta}}\Big]. \tag{51b}$$

3.6. Nonlinear manifold inferred hyperreduction

In the context of reduced-order modeling in FE simulations (see Eq. (17)), the primary computational cost can be attributed to the following cause:

- Evaluating the reduced equations in each global iteration scales with the dimension of the high-fidelity model rather than that of the reduced subspace. This is particularly computationally expensive when assembling $\boldsymbol{K}$ in large-scale simulations, as it requires information from every integration point of the unreduced system. Consequently, this leads to a computational bottleneck, even when advanced MOR techniques are employed.

To overcome this computational bottleneck, hyperreduction techniques Ryckelynck (2005), Farhat et al. (2014, 2015), An et al. (2008) offer an effective solution. The general idea is to evaluate only a few selected elements that are most relevant in the simulations, and compensate for the neglected *virtual work* through the non-negative weighting coefficients. However, capturing the strong nonlinearity induced by local/nonlocal damage remains challenging for classical single-field projection methods, as was shown in prior studies Oliver et al. (2017), Selvaraj and Hallett (2024), Mishra et al. (2024), Zhang et al. (2025a). Therefore, the ECSW-based hyperreduction method proposed by Farhat et al. (2014, 2015) is integrated with the newly developed multi-perspective decomposed quadratic manifold approach proposed in this study. The ECSW method is selected among the various hyperreduction techniques (e.g., ECM[4]

[4] Empirical Cubature Method (ECM).

Hernandez et al. (2017), Lange et al. (2024), Wulfinghoff (2025) or DEIM[5] Radermacher and Reese (2016), Ghavamian et al. (2017), Rutzmoser (2018)) in this study due to its already proven capability in large-scale simulations, ranging from solid to fluid mechanics Farhat et al. (2014), Tezaur et al. (2022), Grimberg et al. (2020), Barnett and Farhat (2022). Using ECSW, the reduced residual vector $\bar{\boldsymbol{R}}_{\text{red}}$, the reduced stiffness matrix $\boldsymbol{K}_{\text{red}}$, as well as the stiffness matrix $\bar{\boldsymbol{K}}_{\text{red}}$ coupled between linear and nonlinear projections are approximated as:

$$\bar{\boldsymbol{R}}_{\text{red}} \approx \sum_{e\in\widetilde{\mathcal{E}}} \xi_e\,(\boldsymbol{L}_e\boldsymbol{\Phi}_{\text{lin}})^{\mathrm{T}}\boldsymbol{R}_e, \quad \boldsymbol{K}_{\text{red}} \approx \sum_{e\in\widetilde{\mathcal{E}}} \xi_e\,(\boldsymbol{L}_e\boldsymbol{\Phi}_{\text{lin}})^{\mathrm{T}}\boldsymbol{K}^e(\boldsymbol{L}_e\boldsymbol{\Phi}_{\text{lin}}), \quad \bar{\boldsymbol{K}}_{\text{red}} \approx \sum_{e\in\widetilde{\mathcal{E}}} \xi_e\,(\boldsymbol{L}_e\boldsymbol{\Phi}_{\text{lin}})^{\mathrm{T}}\boldsymbol{K}^e(\boldsymbol{L}_e\bar{\boldsymbol{\Phi}}_{\text{nonlin}}). \tag{52}$$

Here, the number of selected elements n_s in the hyperreduced mesh $\widetilde{\mathcal{E}}$ is much smaller than the number of elements N_e in the original (unreduced) mesh $\mathcal{E}$, denoted as $n_s = |\widetilde{\mathcal{E}}|$ and $N_e = |\mathcal{E}|$ with $\widetilde{\mathcal{E}} \subseteq \mathcal{E}$ and $n_s \ll N_e$. As expressed in Eq. (52), the stiffness matrix $\bar{\boldsymbol{K}}_{\text{red}}$ composed of linear and nonlinear projections is formulated as a Petrov-Galerkin projection of $\boldsymbol{K}$, due to the fact $\boldsymbol{\Phi}_{\text{lin}} \neq \bar{\boldsymbol{\Phi}}_{\text{nonlin}}$. In Eq. (52), ξ_e denotes a non-negative weighting coefficient associated with the element e, which compensates for the neglected elements to fulfill the equivalence of *virtual work* in the discretized system. $\boldsymbol{L}_e \in \{0,1\}^{n_s\times n}$ represents a Boolean matrix that localizes/selects the corresponding DOFs of an element e from the global high-dimensional vector of unknowns. $\boldsymbol{K}^e$ and $\boldsymbol{R}_e$ are the stiffness matrix and residual vector of the selected element e defined in Eq. (14), respectively. Here, the weighting coefficients associated with the selected elements $\boldsymbol{\xi} = \{\xi_1, \xi_2, \cdots, \xi_e\}$ are determined in an offline training stage at the element level. For a given element e, the reduced residual $\boldsymbol{c}_{je}$ at a certain time step j, along with its accumulated counterpart over time $\boldsymbol{d}_e$, are computed using the reconstructed nodal solution $\boldsymbol{U}'_j$, which is derived from the reduced state $\widetilde{\boldsymbol{U}}_j \in \mathbb{R}^r$. The reduced state $\widetilde{\boldsymbol{U}}_j$ is obtained by solving a nonlinear least-squares problem $\widetilde{\boldsymbol{U}}_j = \arg\min \|\boldsymbol{\Gamma}(\widetilde{\boldsymbol{U}}_j) - \boldsymbol{U}_j\|_2^2$ Barnett and Farhat (2022), Jain and Tiso (2019). All reconstructed snapshots are thus given by $\boldsymbol{U}'_j = \boldsymbol{\Gamma}(\widetilde{\boldsymbol{U}}_j)$. Accordingly, the reduced residual $\boldsymbol{c}_{je}$ and the accumulated residual $\boldsymbol{d}_e$ can be expressed as follows:

$$\boldsymbol{c}_{je} = (\boldsymbol{L}_e\boldsymbol{\Phi}_{\text{lin}})^{\mathrm{T}}\boldsymbol{R}_e(\boldsymbol{U}'_{je}), \quad \boldsymbol{d}_e = \sum_{e\in\widetilde{\mathcal{E}}} \boldsymbol{c}_{je} \quad \Rightarrow \quad \boldsymbol{C} = \begin{pmatrix} \boldsymbol{c}_{11} & \cdots & \boldsymbol{c}_{1e} \\ \vdots & \ddots & \vdots \\ \boldsymbol{c}_{j1} & \cdots & \boldsymbol{c}_{je} \end{pmatrix}, \quad \boldsymbol{d} = \begin{pmatrix} \boldsymbol{d}_1 \\ \vdots \\ \boldsymbol{d}_e \end{pmatrix}. \tag{53}$$

Next, the constructed matrix $\boldsymbol{C} \in \mathbb{R}^{n\,n_{\text{step}}\times n_s}$, which collects the reduced residuals of each element over all time steps, should fulfill the *virtual work* equivalence condition given by:

$$\boldsymbol{C}\,\boldsymbol{\xi} - \boldsymbol{d} = \boldsymbol{0} \quad \text{with} \quad \{\widetilde{\mathcal{E}}, \boldsymbol{\xi}\} = \underset{\{\widetilde{\mathcal{E}},\boldsymbol{\xi}\}}{\arg\min}\{\|\boldsymbol{C}\,\boldsymbol{\xi} - \boldsymbol{d}\|_2^2 \le \tau\|\boldsymbol{d}\|_2^2,\ \boldsymbol{\xi} \ge \boldsymbol{0}\}. \tag{54}$$

Hence, the hyperreduced mesh $\widetilde{\mathcal{E}}$ and its associated weight coefficients $\boldsymbol{\xi}$ are finally being determined by solving Eq. (54) via a sparse non-negative least squares (sNNLS) algorithm Lawson and Hanson (1995), Chapman et al. (2017), Rutzmoser (2018) using a threshold-based early termination criterion. When $\boldsymbol{\xi} = \boldsymbol{1} \in \mathbb{R}^{N_e}$, it means that all elements of the original mesh are selected ($\widetilde{\mathcal{E}} = \mathcal{E}$) with a weight value $\xi_e = 1$ for all elements. The threshold parameter τ is typically chosen to be small, satisfying $0 < \tau \ll 1$, with its specific value determined by the required accuracy of the user and the degree of nonlinearity of the underlying PDEs. As τ decreases, more elements are sampled by the ECSW method to achieve the desired accuracy in reduced-order simulations. Conversely, if τ is set too large, the number of selected elements becomes insufficient to accurately approximate the full-order solution.

Remark 1. $\boldsymbol{c}_{je}$ in Eq. (53) can be constructed using the reduced stiffness matrix $\boldsymbol{c}_{je} = \boldsymbol{T}\,(\boldsymbol{L}_e\boldsymbol{\Phi}_{\text{lin}})^{\mathrm{T}}\boldsymbol{K}^e(\boldsymbol{L}_e\boldsymbol{\Phi}_{\text{lin}}) \in \mathbb{R}^{r^2}$, where $\boldsymbol{T}$ denotes the row-wise vectorization operator that converts a $r\times r$ matrix into a column vector in $\mathbb{R}^{r^2}$, as proposed by Tezaur et al. (2022). This construction is particularly suitable for weakly nonlinear systems where the reduced dimension r remains small (e.g., $r < 20$). However, in the present setting, the number of retained linear modes is defined as $r = k + l + m$, which can lead to a rapid growth in r^2 depending on the choice of parameters k, l, and m. As a consequence, the dimension of $\boldsymbol{c}_{je}$ increases quadratically with r, which can easily lead to a significant computational burden.

Next, the primary task of the Newton-Raphson method is to iteratively compute a suitable global solution vector $\boldsymbol{U} = [\boldsymbol{u}, \bar{\boldsymbol{D}}, \boldsymbol{\theta}]$ by solving the reduced equation $\bar{\boldsymbol{R}}_{\text{red}}\,(\boldsymbol{U}^j_{i+1}) \approx \boldsymbol{0}$, see Fig. 1. Here, j and i denote the time step and iteration number, respectively. Considering a nonlinear projection within the Newton-Raphson scheme Barnett and Farhat (2022), Jain and Tiso (2019), Rutzmoser et al. (2017), the first-order Taylor expansion of the residual in the reduced-order space can be expressed as:

$$\boldsymbol{\Phi}^{\mathrm{T}}_{\text{lin}}\,\boldsymbol{R}\,(\boldsymbol{U}^j_{i+1}) = \boldsymbol{\Phi}^{\mathrm{T}}_{\text{lin}}\,\boldsymbol{R}(\boldsymbol{U}^j_i) + \boldsymbol{\Phi}^{\mathrm{T}}_{\text{lin}}\,\underbrace{\frac{\partial\boldsymbol{R}(\boldsymbol{U}^j_i)}{\partial\boldsymbol{U}^j_i}}_{\boldsymbol{K}}\,\underbrace{\frac{\partial\boldsymbol{U}^j_i}{\partial\Delta\widetilde{\boldsymbol{U}}^j_i}}_{\mathcal{H}}\,\Delta\widetilde{\boldsymbol{U}}^j_{i+1} \approx \boldsymbol{0}, \tag{55}$$

where the global solution vector $\boldsymbol{U}^j_i$ and $\mathcal{H}$ can be expressed as:

$$\boldsymbol{U}^j_i = \boldsymbol{U}^j_{i-1} + \boldsymbol{\Phi}_{\text{lin}}\,\Delta\widetilde{\boldsymbol{U}}^j_i + \bar{\boldsymbol{\Phi}}_{\text{nonlin}}\,\boldsymbol{\Xi}\,\boldsymbol{g}(\Delta\widetilde{\boldsymbol{U}}^j_i), \tag{56a}$$

$$\mathcal{H} = \boldsymbol{\Phi}_{\text{lin}} + \bar{\boldsymbol{\Phi}}_{\text{nonlin}}\,\boldsymbol{\Xi}\,\underbrace{\operatorname{diag}(2\,\Delta\widetilde{\boldsymbol{U}}^j_i)}_{\mathcal{W}}. \tag{56b}$$

[5] Discrete Empirical Interpolation Method (DEIM).

By employing the linear and nonlinear projections as well as the ECSW method, the reduced equations are expressed as:

$$\boldsymbol{\Phi}_{\text{lin}}^{\mathrm{T}}\,\boldsymbol{R}\,(\boldsymbol{U}_{i+1}^{j}) = \boldsymbol{\Phi}_{\text{lin}}^{\mathrm{T}}\,\boldsymbol{R}(\boldsymbol{U}_{i}^{j}) + \boldsymbol{\Phi}_{\text{lin}}^{\mathrm{T}}\,\boldsymbol{K}\,(\boldsymbol{\Phi}_{\text{lin}} + \bar{\boldsymbol{\Phi}}_{\text{nonlin}}\,\Xi\,\mathcal{W})\,\Delta\widetilde{\boldsymbol{U}}_{i+1}^{j}, \tag{57}$$

$$\underbrace{\boldsymbol{\Phi}_{\text{lin}}^{\mathrm{T}}\,\boldsymbol{R}(\boldsymbol{U}_{i}^{j})}_{:\approx\bar{\boldsymbol{R}}_{i,\text{red}}^{j}} + \underbrace{\boldsymbol{\Phi}_{\text{lin}}^{\mathrm{T}}\,\boldsymbol{K}\,\boldsymbol{\Phi}_{\text{lin}}}_{:\approx\boldsymbol{K}_{i,\text{red}}^{j}}\,\Delta\widetilde{\boldsymbol{U}}_{i+1}^{j} + \underbrace{\boldsymbol{\Phi}_{\text{lin}}^{\mathrm{T}}\,\boldsymbol{K}\,\bar{\boldsymbol{\Phi}}_{\text{nonlin}}}_{:\approx\bar{\boldsymbol{K}}_{i,\text{red}}^{j}}\,\Xi\,\mathcal{W}\,\Delta\widetilde{\boldsymbol{U}}_{i+1}^{j} \approx \boldsymbol{0}, \tag{58}$$

$$\Delta\widetilde{\boldsymbol{U}}_{i+1}^{j} = -(\boldsymbol{K}_{i,\text{red}}^{j} + \bar{\boldsymbol{K}}_{i,\text{red}}^{j}\,\Xi\,\mathcal{W})^{-1}\,\bar{\boldsymbol{R}}_{i,\text{red}}^{j}, \tag{59}$$

$$\boldsymbol{U}_{i+1}^{j} = \boldsymbol{U}_{i}^{j} + \boldsymbol{\Phi}_{\text{lin}}\,\Delta\widetilde{\boldsymbol{U}}_{i+1}^{j} + \bar{\boldsymbol{\Phi}}_{\text{nonlin}}\,\Xi\,\boldsymbol{g}(\Delta\widetilde{\boldsymbol{U}}_{i+1}^{j}), \tag{60}$$

$$\left\|\bar{\boldsymbol{R}}_{\text{red}}(\boldsymbol{U}_{i+1}^{j})\right\| \leqslant tol, \tag{61}$$

$$i \leftarrow i+1. \tag{62}$$

As observed in Eq. (58), utilizing the inverse of the reduced stiffness matrices in Eq. (59) leads to a noticeable reduction in computational complexity due to the lower dimension of both $\boldsymbol{K}_{\text{red}}$ and $\boldsymbol{K}$ compared to those of full-order simulations. Note that Eq. (58) incorporates not only the traditional linear term $\boldsymbol{K}_{\text{red}}$ but also the additional enrichment from the quadratic approximation terms: $\bar{\boldsymbol{K}}_{\text{red}}$, Ξ, and $\mathcal{W}$. In some cases, a regularization $\gamma_s\,\boldsymbol{I}_r$ is needed to add to the reduced stiffness matrix to avoid numerical singularities, where γ_s is a tiny value (e.g., 10^{-9}). These quantities are crucial to achieve a higher accuracy compared to the classical POD throughout the iteration process.

It should be mentioned at this point that the proposed technique in this study is rooted in an extended application of the proper orthogonal decomposition method to the linearized expression of the global residual vector. This is due to the finite element discretization and differs from other cases in which classical reduced-order modeling techniques based on Galerkin projection are applied. When linearizing the global residual vector, nonlinear contributions do not only arise from the stiffness matrix coupled with the linear and nonlinear projection matrices, but also from the coefficient matrix (see Eq. (58)). These nonlinearities are of quadratic type, as inferred from the manifold approach. To the end, when the norm of the reduced residual $\bar{\boldsymbol{R}}_{\text{red}}$ falls below a predefined tolerance (tol), the converged increment in the reduced-order solution $\Delta\widetilde{\boldsymbol{U}}$ is deemed found. Simultaneously, the reduced solution is projected back into the full-order equation system to update the solution vector $\boldsymbol{U}$ throughout the iteration process.

In summary, a fundamental characteristic of the framework proposed in this study is the integration of the developed multi-field decomposed quadratic manifold method with an ECSW-based hyperreduction scheme, as described in subsections 3.4 and 3.6, respectively. The numerical example used to illustrate this feature of the model is presented in Test 1 (subsection 4.1). Moreover, the multi-state decomposition introduced in subsection 3.5 is extended to construct two physical state-based projection matrices (i.e., the linear and nonlinear projection matrices) for predictive simulations. It is important to note that these projection matrices are exclusively employed for the predictive simulations in Test 2 (subsection 4.2). The integration of the multi-field and multi-state methods into a new *multi-perspective* method constitutes a fundamental aspect of the theoretical framework developed in this work.

3.7. Measurement of accuracy and computational cost

To enable a clear comparison between reduced- and full-order simulations in terms of both computational accuracy and efficiency, two measurement quantities are defined: the relative error (ε_r) and two CPU time ratios (η_s and η_w). η_s and η_w denote the CPU time ratios for solving the global equation system, excluding and including the element assembly time, respectively:

$$\varepsilon_r = \frac{1}{N}\sum_{j=1}^{N}\frac{|u_{p,\text{red}}^{j} - u_{p,\text{full}}^{j}|}{|u_{p,\text{full}}^{j}|}, \quad \eta_s = \sum_{j=1}^{N}\frac{T_{\text{red},s}^{j}}{T_{\text{full},s}^{j}}, \quad \text{and} \quad \eta_w = \sum_{j=1}^{N}\frac{T_{\text{red},w}^{j}}{T_{\text{full},w}^{j}} \tag{63}$$

Here, N represents the actual number of time steps. $u_{p,\text{red}}^{j}$ and $u_{p,\text{full}}^{j}$ denote the considered displacement components obtained using the reduced and full-order model at a selected nodal point p at time j. $T_{\text{red},s}^{j}$ and $T_{\text{full},s}^{j}$ are the solution time costs of the reduced and full order models at time j, without counting the assembly time, respectively. $T_{\text{red},w}^{j}$ and $T_{\text{full},w}^{j}$ are the wall-time costs of the reduced and full-order models at time j, respectively. The smaller the CPU time ratios η_s and η_w, the better the performance of the reduced-order model becomes. In the context of nonlocal damage, a relative error measure is unsuitable, since a division by zero occurs in undamaged regions of the structure. On account of this issue, an absolute error in damage ε_a is adopted in this study to quantify the accuracy of the nonlocal damage field:

$$\varepsilon_a = \frac{1}{N}\sum_{j=1}^{N}|\bar{D}_{p,\text{red}}^{j} - \bar{D}_{p,\text{full}}^{j}|. \tag{64}$$

Here, $\bar{D}_{p,\text{red}}^{j}$ and $\bar{D}_{p,\text{full}}^{j}$ represent the nonlocal damage variables at a selected nodal point p at time j, computed using the reduced-order and full-order models, respectively.

4. Numerical examples

In the following, several three-dimensional numerical examples are employed to investigate the performance of the newly developed multi-field and multi-state decomposed nonlinear manifold MOR approach. The material model in this study and its solver are implemented in *FEAP* Taylor (2014) and *Python*, respectively. All contour plots are shown using the open-source software *Paraview* Ahrens et al. (2005).

4.1. Test 1: Rectangular specimen

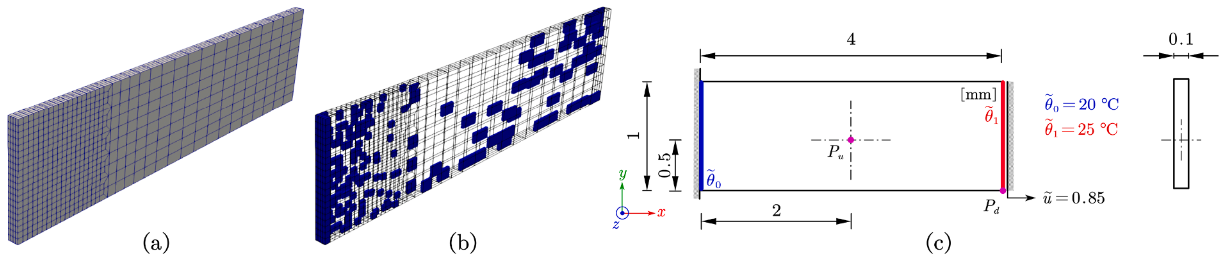

Fig. 3. (a) Schematic illustration of the meshed rectangular specimen. The prescribed displacement on the right surface is $\widetilde{u} = 0.85$ mm. Different constant temperatures are prescribed on the left and right surfaces with $\widetilde{\theta}_0 = 20\,°\mathrm{C}$ and $\widetilde{\theta}_1 = 25\,°\mathrm{C}$, respectively. Points P_u and P_d are selected to compare the error of both the displacement component u and temperature θ, as well as nonlocal damage variable $\bar{D}$, respectively; (b) selected ECSW elements (shown in blue) with $n_s = 245$ elements over a meshed discretization of 2240 elements; (c) geometry and considered boundary value problem.

Table 1
Material and regularization parameters as well as their corresponding equations.

Symbol	Parameter description	Value	Unit	Eq.
Elastic parameters				
Λ	1st Lamé constant	25,000	MPa	(4)
μ	2nd Lamé constant (shear modulus)	55,000	MPa	(4)
Plastic parameters				
σ_{y0}	initial yield stress	100	MPa	(A.9)
a	kinematic hardening parameter	62.5	MPa	(5)
P	linear isotropic hardening parameter	0	MPa	(5)
e_p	1st nonlinear isotropic hardening parameter	125	MPa	(5)
f_p	2nd nonlinear isotropic hardening parameter	5	-	(5)
Damage parameters				
Y_0	initial damage threshold	2.5	MPa	(A.9)
e_d	1st damage hardening parameter	5.0	MPa	(6)
f_d	2nd damage hardening parameter	100	-	(6)
A	gradient damage parameter	75	MPa mm^2	(7)
H	micromorphic penalty parameter	10^6	MPa	(7)
Thermal parameters				
c	volumetric heat capacity	3.59	mJ/(mm^3 K)	(13)
α	thermal expansion coefficient	1.1	10^{-5}/K	(1)
K_0	initial heat conductivity	50.2	mW/(mm K)	(A.7)
θ_0	reference temperature	273.15	K	(1)
ω	thermal softening parameter	0.002	1/K	(A.8)
Regularization parameters				
γ_u	regularization parameter for displacement	3.0	-	(39)
$\gamma_{\bar{D}}$	regularization parameter for damage	1.0	-	(39)
γ_θ	regularization parameter for temperature	3.0	-	(39)

In this section, Test 1 is designed to investigate the performance of the developed multi-field decomposed nonlinear manifold MOR approach for fully thermo-mechanically coupled damage-plasticity simulations without using the multi-state decomposition method, see Fig. 3. The specimen is discretized by linear 8-node hexahedral elements[6], resulting in a total number of 2240 elements. The thickness direction of the specimen is meshed with four elements. Each node possesses five degrees of freedom: three displacement components (u, v, and w), nonlocal damage $\bar{D}$, and temperature θ. The errors between the reduced- and full-order simulations associated with displacement and nonlocal damage fields are evaluated at the selected points P_u (2, 0.5, 0) and P_d (4, 0, 0), respectively.

[6] An 8-node hexahedral element possesses a linear shape function for all considered corresponding fields in this study.

The temperatures on the left and right surfaces of the specimen are prescribed by constant values of $\widetilde{\theta}_0 = 20\,°\mathrm{C}$ and $\widetilde{\theta}_1 = 25\,°\mathrm{C}$, respectively. More details on the boundary conditions are given in Fig. 3. The simulation is carried out in 100 timesteps. Mechanical and thermal parameters are taken from Brepols et al. (2020) and Dittmann et al. (2020), respectively, see Table 1.

4.1.1. Comparison of singular values for different fields

As shown in Fig. 4(a), the normalized singular values of the displacement, temperature, and damage fields exhibit a quite slow decay, indicating that the solution manifold of this fully thermo-mechanically coupled damage-plasticity problem resists an efficient reduction via linear projection, due to the Kolmogorov barrier. Notably, the normalized singular values of the damage field stabilize as the number of modes exceeds approximately 90. This stabilization results from the natural value interval of the nonlocal damage, which lies between 0 and 1 to distinguish undamaged and fractured phases. When the specimen is fractured, the material's stiffness is almost fully degraded and the nodal damage variables remain nearly constant. From this point on, increasing the number of modes yields negligible improvement, and the accuracy of the reduced-order model related to the damage field saturates. Moreover, to better understand the projection characteristics in the damage field, Fig. 5 presents the first seven POD modes corresponding to the damage variable.

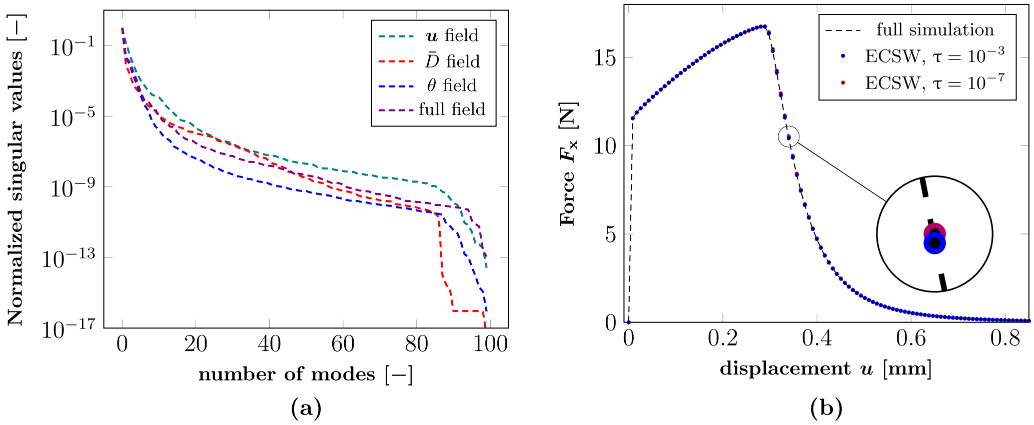

Fig. 4. (a) Normalized singular values in the case of the multi-field decomposed MOR approach and the classical non-decomposed MOR approach (full field); (b) force-displacement curve comparison between the full-order simulation and the reduced-order simulation using nonlinear manifold-based ECSW with different tolerances τ.

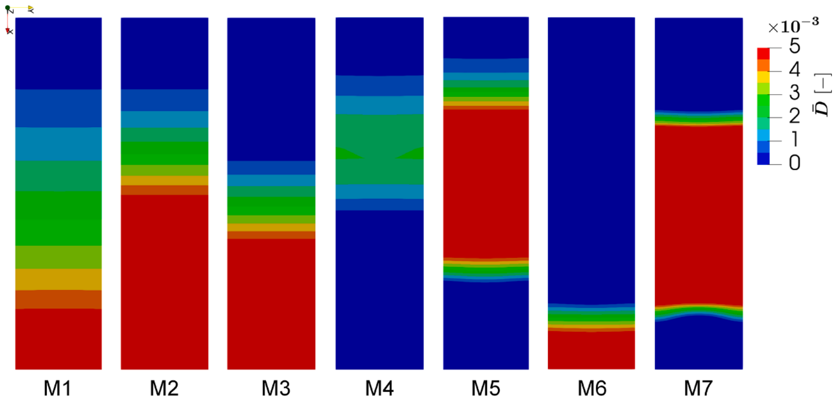

Fig. 5. Distribution of the first seven POD modes for the nonlocal damage of the non-notched specimen.

In Fig. 4(b), a comparison of the force-displacement curves between the full-order simulation and the reduced-order simulation is shown. The numbers of linear and nonlinear modes used for the reduced-order simulations are selected as 90 and 5 for the three fields, respectively. As can be seen, the newly developed multi-field decomposed nonlinear manifold approach agrees very well with the full-order simulation in terms of the force-displacement curve, even though a pretty small number of selected elements ($n_s = 245$ for $\tau = 10^{-3}$; $n_s = 365$ for $\tau = 10^{-7}$) is used.

4.1.2. Influence of ECSW's tolerance τ on the accuracy

After obtaining an accurate ROM from subsection 4.1.1 using predefined ECSW tolerances, it is essential to assess how the chosen tolerance affects the accuracy of the developed ROM. Therefore, the influence of the ECSW training tolerance τ on the accuracy of the reduced-order simulations is systematically investigated in this section. The parameter τ is varied from 5×10^{-8} to 10^{-3}. As shown in Fig. 6(a), the displacement component u, the nonlocal damage variable $\bar{D}$, and the temperature variable θ obtained from the reduced-order simulations are compared with their corresponding full-order results. To provide a more intuitive visualization, contour plots comparing between the full-order and reduced-order fields are presented in Fig. 8. Since the contour patterns of the nonlocal damage field are similar to those of the temperature field, only the latter are displayed. Furthermore, to further clarify how the number of selected modes affects the ECSW offline training process, the number of elements selected by the ECSW is investigated using different numbers of modes for k, l, and m, as well as varying the training tolerances. The corresponding results are shown in Fig. 7(a).

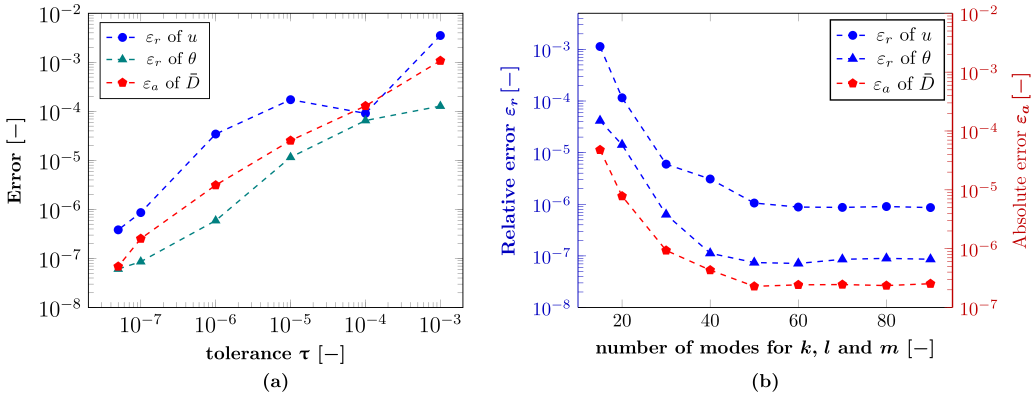

Fig. 6. (a) Error depending on ECSW's training tolerance τ varied from 5×10^{-8} to 10^{-3}; (b) error depending on the number of linear modes per field from 15 to 90. The employed tolerance and the number of nonlinear modes per field are set to $\tau = 10^{-7}$ and $q = 5$, respectively.

As shown in Fig. 6(a), the errors decrease for the different fields while decreasing the ECSW tolerance τ. This phenomenon is attributed to an increase in the number of selected evaluation elements, which enhances the approximation accuracy of the reduced-order model by providing a richer sampling. However, incorporating more elements inevitably increases the computational cost during the assembly and evaluation phases. Furthermore, setting a higher value for the tolerance sacrifices accuracy to obtain a higher computational efficiency. Therefore, selecting an appropriate ECSW's tolerance for multiphysics damage simulations requires careful consideration of practical engineering requirements as well as a balance between computational accuracy and efficiency. Fig. 6(b) reveals an expected key trend: increasing the number of linear modes brings a better precision for the different fields. However, beyond roughly 50 modes in each field, the error reaches a plateau, meaning that further increasing the number of modes does not lead to a higher accuracy anymore while incurring unnecessary computational cost. Therefore, 50 linear modes and 5 nonlinear modes per field are sufficient to ensure both stability and accuracy for the reduced-order simulation in Test 1.

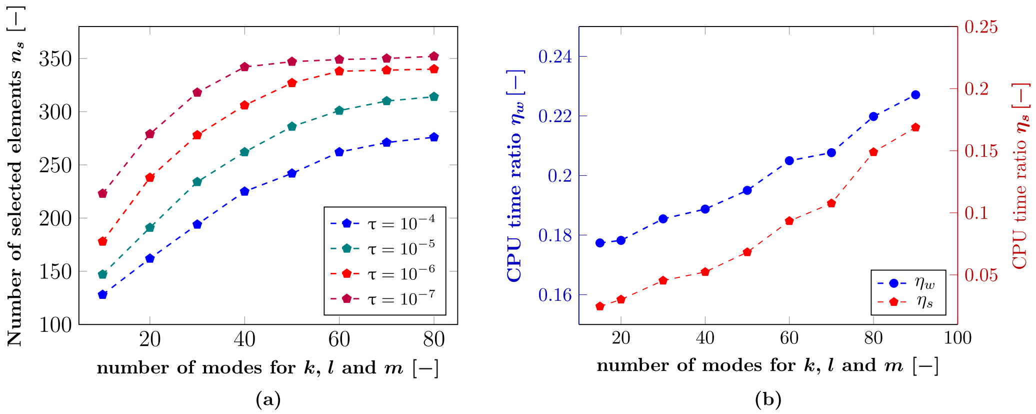

Fig. 7. (a) Comparison of the number of selected ECSW elements for different numbers of modes for k, l, and m; (b) CPU time ratio comparison for different numbers of linear modes for the displacement field, nonlocal damage field, and temperature field using the ECSW and nonlinear projection-equipped reduced-order simulations. The employed ECSW's tolerance is $\tau = 10^{-7}$.

Here, both the wall-time ratio η_w and the solution time ratio η_s are employed to evaluate the performance of the proposed reduced-order model while varying the number of linear modes from 15 to 90, see details about the definition of the CPU time ratio in Eq. (63). The number of linear modes r is varied instead of q because r predominantly determines the dimension of the reduced equation system, which significantly influences the computational efficiency in reduced-order simulation, see Eq. (52). As shown in Fig. 7(b), the reduction is more pronounced for the solution time ratio due to the quadratic manifold's capacity to accurately capture nonlinear behavior using a few numbers of modes. The wall-time ratio is more sensitive to the number of selected elements in the ECSW procedure. For Test 1, a relatively larger number of elements is required in comparison to simulations involving weakly nonlinear materials (e.g., hyperelastic models de Parga et al. (2023), Rutzmoser and Rixen (2017)), owing to the higher complexity and nonlinearity of the present damage model, which leads to global softening in the structure and thus demands a denser sampling to fulfill the accuracy.

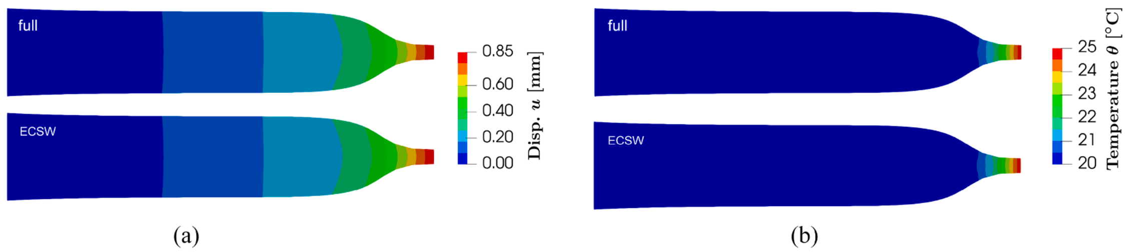

Fig. 8. (a) Comparison of contour plots for the displacement component u between full-order and reduced-order simulations, where the employed numbers of linear modes per field are set to 90. The number of selected ECSW elements and the corresponding tolerance τ are selected as $n_s = 365$ and 10^{-7}, respectively. (b) Comparison of contour plots for the temperature θ between full-order and reduced-order simulations.

4.2. Test 2: HC specimen

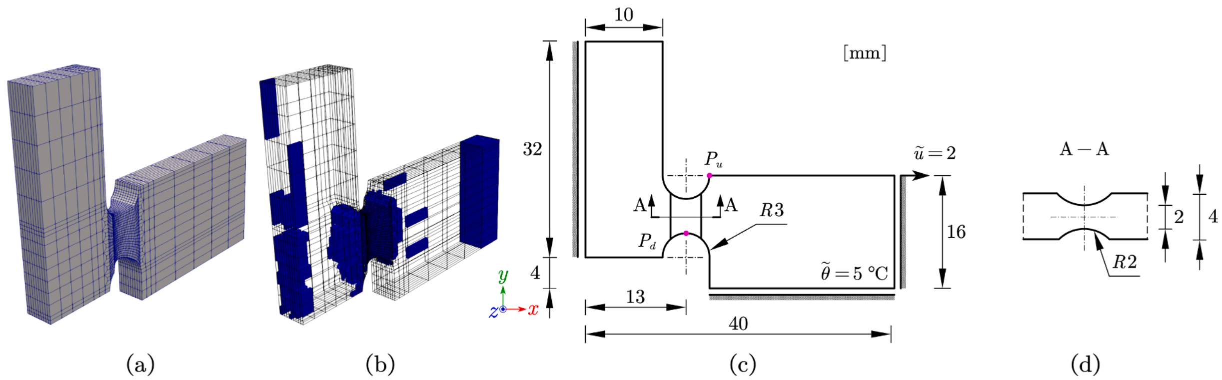

Fig. 9. Schematic illustration of the HC specimen and the considered boundary value problem; (a) meshed HC specimen; (b) selected ECSW elements (shown in blue with $n_s = 2106$ elements) for a mesh discretization of 10,730 elements; (c) dimension and boundary conditions of HC specimen taken from Wei et al. (2023, 2024); (d) cross-section of HC specimen at section A-A.

As shown in Test 1 (subsection 4.1), the developed multi-field decomposed ROM accurately reproduces the full-order simulation results. To fully demonstrate its practical relevance, the ROM is further employed for predictive applications. Hence, Test 2 is conducted on an HC specimen in accordance with the experimental setup outlined by Wei et al. (2023, 2024), under a constant temperature of $\tilde{\theta} = 5\,°\text{C}$, see Fig. 9. On the right surface of the specimen, a displacement is prescribed in x direction with a value of $\tilde{u} = 2$ mm. Note that, due to symmetry, only a quarter of the structure is used and shown in Fig. 9. To investigate the precision of the reduced-order simulation, points $P_u\,(16,\,16,\,4)$ and $P_d\,(13,\,7,\,2)$ are selected to measure the nodal values of displacement component u and nonlocal damage $\bar{D}$, respectively.

4.2.1. Multi-state and multi-field decomposed MOR for prediction

This part employs the developed multi-field and multi-state decomposed quadratic manifold MOR approach and assesses its predictive performance for multiphysics damage-plasticity simulations. Two full-order simulations are conducted with a deviation of $\pm 50\%$ in the Lamé constants, as shown in Table 1. Subsequently, the linear and nonlinear predictive projection matrices are derived along with the coefficient matrix. As detailed in Section 3.5, the simulation process for the tensile test of the HC specimen is decomposed into the elastic, hardening, and softening phases. Numbers of snapshots selected for the elastic, hardening, and softening states are specified as 4, 28, and 114, respectively, based on the overall mechanical performance in the simulations. As illustrated in Fig. 10(a), the dominant contribution in the elastic region is primarily governed by the displacement field, without an influence from the damage field. A relatively small influence of the temperature field can be expected, since it is set constant. This behavior is attributed to the slower decay of normalized singular values in the displacement field compared to those in the temperature field.

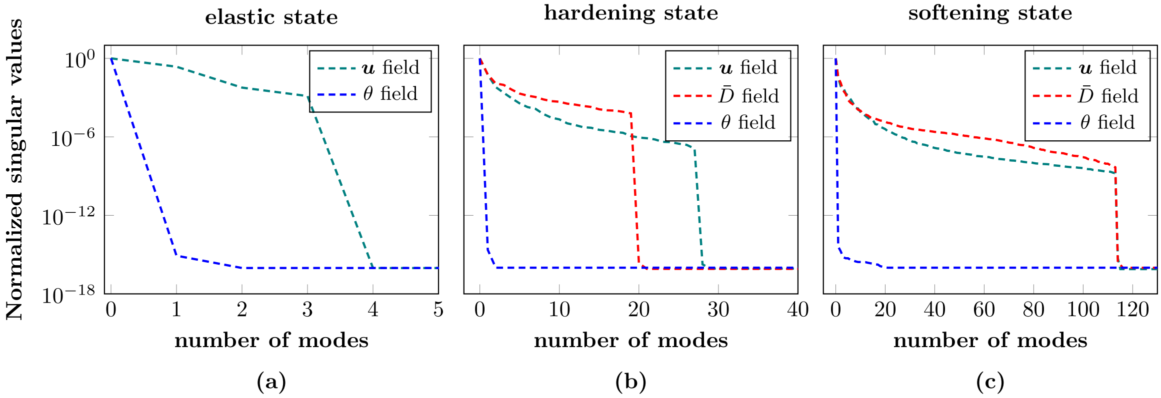

Fig. 10. Normalized singular values using the proposed multi-field and multi-state decomposition approach for a mesh discretization of 10,730 elements in (a) elastic, (b) plastic hardening, and (c) softening states.

The fast decay of singular values in the temperature field stems from the constant temperature throughout the specimen, which can be effectively represented using only a few numbers of temperature modes. A similar trend is also observed in Figs. 10 (b) and (c).

Next, the focus turns to the distribution of the normalized singular values associated with the nonlocal damage field. These values are not shown in Fig. 10(a) because the nonlocal damage variable remains inactive during the elastic phase. At this stage, the evolution of the local damage variable is governed by the damage threshold at the integration point level and remains zero, unless the damage-driving force Y exceeds the critical threshold Y_0, see Eq. (A.9). Due to the penalization strategy coupling the local and nonlocal damage variables, the nonlocal damage field is also identically zero. Under these conditions, the corresponding damage projection matrices are not needed to approximate the nonlocal damage variable (see Eq. (6)).

One interesting observation in Fig. 10(b) is that the influence of the nonlocal damage field on the material's hardening response does not persist throughout the process. This is reflected in the rapid decay of its normalized singular values that drop to near-zero at 20 modes, even though 28 snapshots are collected to formulate the entire hardening phase. This phenomenon highlights two aspects in this example when selecting the number of modes for reduced-order modeling. From a computational perspective, only a relatively small number of nonlocal damage modes is needed to accurately capture the deformation-induced hardening behavior of the HC specimen. This enables a more efficient selection of modes across different physical fields to improve the overall computational performance in reduced-order simulations. From a physical perspective, the displacement field primarily governs the thermo-mechanically coupled hardening response in Test 2, whereas the nonlocal damage and temperature fields play a comparatively minor role.

By contrast, Fig. 10(c) shows that the distribution of the normalized singular values for both the damage and displacement fields persists longer during the softening phase, where the corresponding singular values decay more slowly. These fields exhibit dominant modal contributions, highlighting their critical role in the evolution of damage. This observation is in agreement with physical expectations: the initialization and evolution of damage are strongly related to strain localization, where the local damage variable governs the degradation of stress-like quantities, such as the second Piola-Kirchhoff stress $\mathbf{S}$, Mandel stress $\boldsymbol{M}$, and back-stress tensors χ, while the nonlocal damage field enforces spatial regularity. Therefore, a larger number of modes is required in these fields to accurately capture the complex interactions associated with damage-induced softening. To evaluate the predictive performance of the reduced-order model, Fig. 11(a) compares the force-displacement responses obtained from both reduced- and full-order simulations. The reference solution is additionally computed without any deviation in the Lamé constants in order to provide a consistent baseline for assessing the accuracy of the reduced model.

As shown in Fig. 11(a), the proposed multi-field and multi-state decomposition technique leads to a good predictive performance across the entire simulation process. The evolution of the nonlocal damage in the reduced-order simulation is illustrated in Fig. 12, while Fig. 11(b) presents the corresponding absolute error in the predictive scenario. In addition, as the number of displacement modes k exceeds 33, the predictive error stabilizes at approximately 5.74×10^{-5}. At this level of accuracy, discrepancies in the force-displacement curves and contour plots become visually indistinguishable, see Fig. 11(a). Importantly, the employment of the multi-state decomposed nonlinear manifold enables a stabilized error with a certain number of modes. These results collectively demonstrate the robustness and reliability of the proposed multi-field and multi-state decomposed nonlinear manifold MOR approach for mitigating the Kolmogorov barrier in damage.

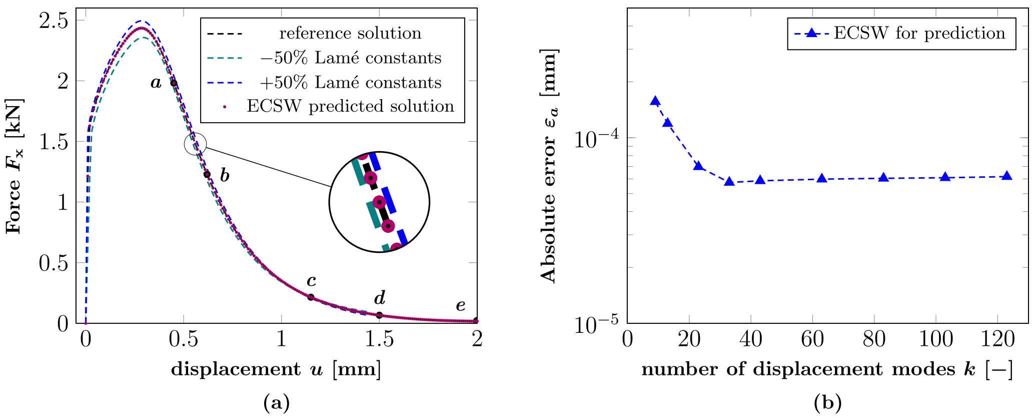

Fig. 11. (a) Force-displacement curves, comparing the reference solution to the predicted result using ECSW for the HC specimen. The number of displacement modes in the predictive simulation for the displacement field is selected as $k = 33$, whereas the corresponding mode numbers for nonlocal damage and temperature fields are defined as $l = 120$ and $m = 2$, respectively; (b) the predictive error in displacement component u for different numbers of displacement modes k.

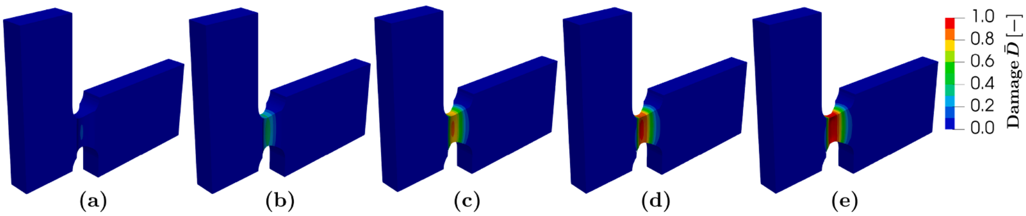

Fig. 12. A schematic illustration of the nonlocal damage evolution in a reduced-order simulation for the HC specimen. The corresponding numbers of modes are $k = 33$, $l = 120$, and $m = 2$. The associated figures depict the specimen's state at loading displacements of $u = 0.45$, 0.62, 1.15, 1.50, and 2.00 mm, as indicated by points a, b, c, d, and e in Fig. 11(a).

5. Results and discussion

5.1. Decomposed versus non-decomposed nonlinear manifold MOR

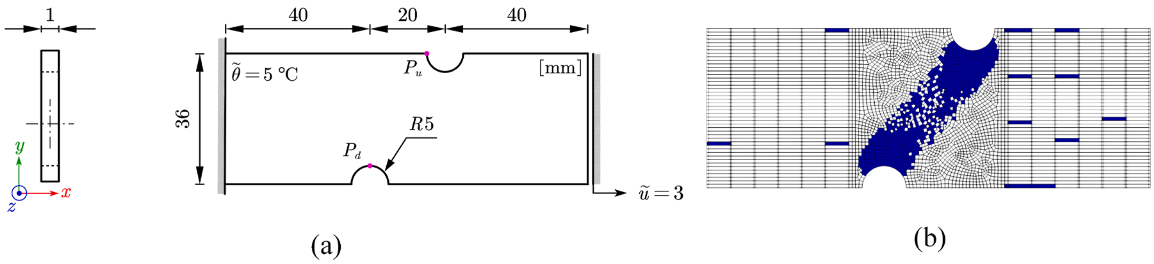

Fig. 13. (a) Schematic illustration of an asymmetrically notched specimen and the considered boundary value problem. The displacement in the horizontal direction on the right surface is prescribed by a value of $\tilde{u} = 3$ mm. A constant temperature is prescribed on the specimen $\tilde{\theta} = 5$ °C. Points P_u and P_d are selected to compare the errors of the displacement and nonlocal damage variables, respectively. The thickness direction is constrained. (b) The selected ECSW elements ($n_s = 708$) are shown in blue in a discretized specimen of 2912 elements.

As shown in Eqs. (38) and (39), a novel decomposed strategy is proposed in the optimization process in order to obtain a more accurate coefficient matrix $\boldsymbol{\Xi}$ in the context of the quadratic manifold approach. Here, a comparative analysis is performed for an asymmetrically notched specimen (Fig. 13) to assess the performance of the developed method. The distribution of normalized singular values for the asymmetrically notched specimen is shown in Fig. C.17. The objective of subsection 5.1 is to investigate the influence of the field decomposition technique on the coefficient matrix, when the objective function is optimized in terms of the Frobenius norm in Eq. (39). For the sake of simplicity, the specimen thickness is discretized using a single element.

To evaluate the accuracy of the reduced-order simulations, both the absolute error and the relative error are computed. As illustrated in Fig. 14(a), the number of linear displacement modes is chosen as $k = 15$, while the number of nonlinear displacement

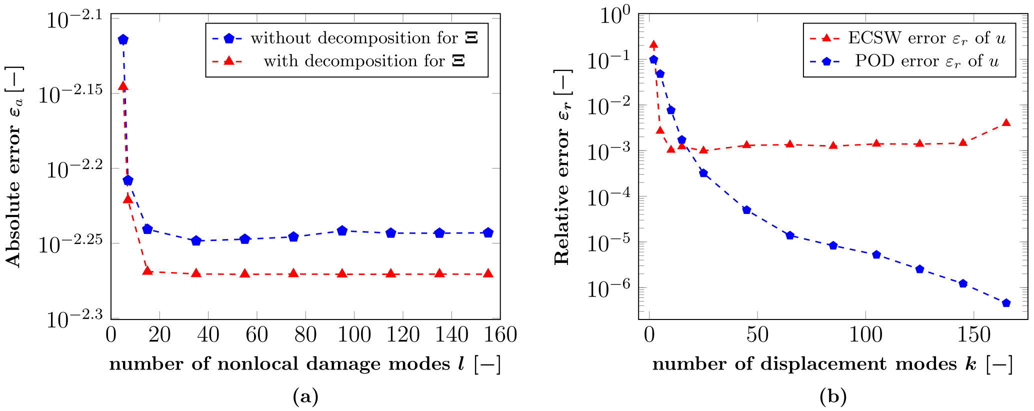

Fig. 14. (a) Absolute errors for different numbers of linear nonlocal damage modes $l \in [5, 155]$ using a mesh discretization of 2912 in the case with and without the field decomposition method. (b) Error comparison for different numbers of linear displacement modes $k \in [2, 165]$ for a mesh discretization of 8979 elements, with $l = 150$ linear and $q_l = 5$ nonlinear modes for the nonlocal damage field, $q_k = 5$ nonlinear modes for the displacement field, $m = 2$ linear and $q_m = 1$ nonlinear modes for the temperature field.

modes is set to $q_k = 5$. For the temperature field, both the number of linear and the nonlinear temperature modes are selected as $m = 2$ and $q_m = 1$, respectively. Moreover, the number of linear nonlocal damage modes varies within the range $l \in [5, 155]$, and the number of nonlinear damage modes is fixed to $q_l = 5$. The results shown in Fig. 14(a) highlight that the field decomposition technique outperforms the non-decomposed method with respect to the error in the nonlocal damage variable. This advantage becomes increasingly significant for k ranging from 2 to 165, as illustrated in Fig. 14(b), which compares the POD-based and ECSW-based nonlinear manifold methods. As can be observed and could be expected, the error of the ECSW-based nonlinear manifold approach is higher than the error of the POD-based nonlinear manifold approach. This aligns with the trend observed in comparisons between POD- and hyperreduction-based methods that make use of linear projection techniques by Radermacher and Reese (2016). The reason for this lies in the hyperreduction technique's selection of only a few effective elements aimed at significantly accelerating simulations. However, this naturally leads to an impact on the accuracy Jain (2019), Rutzmoser (2018). The goal in engineering problems is usually to find a suitable compromise between computational efficiency and accuracy, see Fig. 15(a). Although the computational cost can be significantly reduced by evaluating only a small subset of elements, this efficiency inherently comes at the expense of accuracy, due to the difficulty of accurately representing complex constitutive behavior with such a limited sampling.

5.2. *Influence of the number of linear displacement modes in the nonlinear manifold approach*

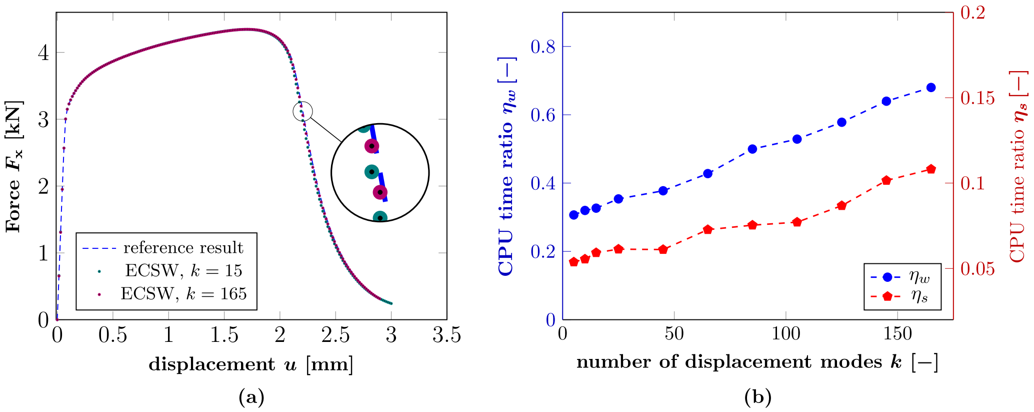

Fig. 15. (a) Force-displacement curves comparison between full-order and reduced-order simulations for a fixed discretization of 8979 elements with $k = \{15, 165\}$. (b) CPU time ratio comparison for different values of k using ECSW and nonlinear manifold-equipped reduced-order simulations.

Fig. 15(a) presents a comparison of the force-displacement curves for different values of $k = \{15, 165\}$. Using the nonlinear manifold ECSW method, the computed error in the nonlocal damage field reaches 4.51×10^{-3}. This level of accuracy, achieved with relatively low values for k, is difficult to achieve using a linear approximation approach, unless the number of modes is significantly increased, e.g., to $k \geq 40$ Zhang et al. (2025a). In return, this would lead to a substantial rise in computational cost. These results demonstrate that, even with a relatively small number of modes, the nonlinear manifold ECSW can lead to good performance. Fig. 15(b) shows the change in the CPU time ratio concerning both η_w and η_s, when the number of displacement modes k increases for a fixed mesh discretization of 8979 elements.

5.3. Comparisons between linear and nonlinear manifold approaches

A comparison between the linear and quadratic approximation techniques is conducted to illustrate the computational barrier posed by the linear approach in damage-induced problems, which is attributed to the slow decay (see Appendix C) in the Kolmogorov n-width. This comparison assesses both the relative error and the associated computational cost. To allow for a consistent comparison with the multi-field decomposed linear manifold approach recently proposed by Zhang et al. (2025a), the mode numbers are prescribed as $l = 155$ for the nonlocal damage field and $m = 5$ for the temperature field. The number of nonlinear modes is set to the same value as in subsection 5.1.

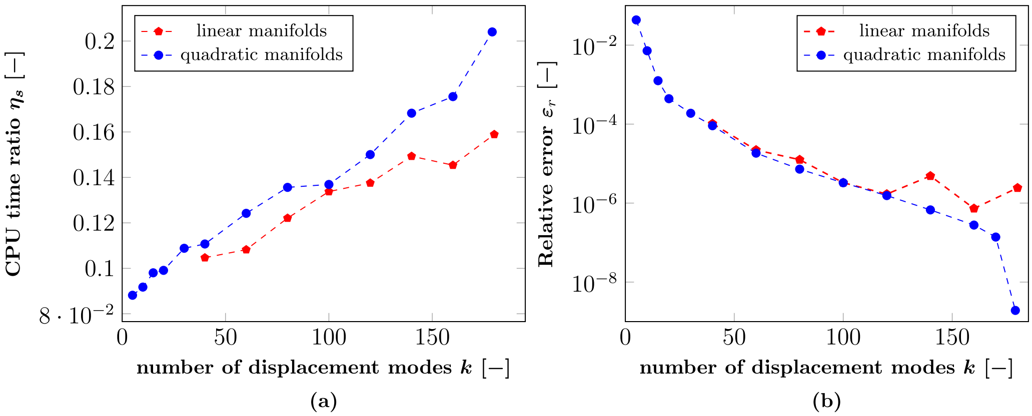

Fig. 16. Comparisons between linear and nonlinear manifold MOR approaches without using ECSW in terms of (a) the CPU time ratio η_s in solving the equation system and (b) the relative error ε_r for a mesh discretization of 2912 elements.

Typically, a fast reduced-order simulation is realized by choosing a low number of modes for a target equation system. However, in the context of damage-plasticity simulations under complex shear and tensile loadings, a linear projection often results in an ill-conditioned equation system, here observed when less than 40 displacement modes are used, as shown in Fig. 16. This limitation is in agreement with the Kolmogorov barrier in approximation theory, whereby iteration is prematurely terminated due to non-convergence. In contrast to the linear projection, the relative error ε_r associated with the nonlinear projection decreases smoothly and monotonically as the number of linear modes increases. As observed in Fig. 16(b), the linear projection method also exhibits significant error fluctuations at higher numbers of modes (e.g., $k \geq 135$). In contrast, the quadratic manifold approach leads to stable results across a wide range of modes. This behavior reflects the capacity of nonlinear projections to approximate the strong nonlinearities present in thermo-mechanically coupled damage-plasticity simulations. It also indicates a significant reduction in the approximation barrier commonly encountered for linear approximations. Nevertheless, the nonlinear projection comes at the price of additional computational cost compared to the linear projection, as shown in Fig. 16(a). This can be mitigated when integrating the ECSW technique into the quadratic manifold method. Since the dimension of the equation system will be small enough to neglect the computational cost of nonlinear operations. In conclusion, the key advantage of nonlinear projection lies in its capacity to mitigate the Kolmogorov n-width barrier in linear approximation, thereby enabling accurate and stable reduced-order simulations with a very small number of dominant modes.

6. Conclusion

In this study, a unified multi-perspective (multi-field and multi-state) quadratic manifold-based model order reduction framework has been proposed to mitigate the approximation barrier caused by the slow decay of the Kolmogorov n-width in thermo-mechanically coupled damage-plasticity simulations. To further enhance computational efficiency for solving the highly nonlinear equation systems, the framework integrated the ECSW hyperreduction method, which allows accurate results to be achieved using only a small subset of selected elements and modes.

A key contribution of this work lies in the newly developed multi-field and multi-state decomposition strategy, which is grounded in the material's physical states to guide the selection of mode numbers for each coupled field. Comparative analyses have demonstrated that, unlike the classical linear manifold approach, which often suffers from premature stagnation in reduced-order simulations, the proposed multi-perspective quadratic manifold approach ensured a smooth and monotonic decrease for the computed error as the number of modes increases, thereby effectively mitigating the Kolmogorov barrier.

Another important characteristic of the proposed framework is its capability to effectively decouple material states and physical fields in complex damage-involved multiphysics problems. This decoupling has provided a clearer assessment of how each individual field contributes to and interacts within the overall multiphysics behavior, as shown through the normalized singular value distributions of the coupled solutions. In addition, a systematic study of the ECSW training tolerances has revealed that the number of selected elements played a critical role in balancing accuracy and computational efficiency for damage-involved multiphysics simulations.

Despite the demonstrated effectiveness of the proposed framework in mitigating the Kolmogorov barrier, its dependence on a fixed discretization remains an inherent limitation of global Galerkin-projection-based MOR techniques. Furthermore, this study has focused exclusively on monotonically increasing loadings leading to structural failure. Extending the approach to address high-cycle fatigue-induced damage under multiphysics scenarios could open a broad avenue for future work, with significant potential for industrial applications, such as fatigue-life prediction and durability assessment.

CRediT authorship contribution statement

Qinghua Zhang: Writing – review & editing, Writing – original draft, Visualization, Validation, Supervision, Software, Resources, Project administration, Methodology, Investigation, Formal analysis, Data curation, Conceptualization; **Stephan Ritzert:** Writing – review & editing, Methodology; **Jian Zhang:** Writing – review & editing; **Jannick Kehls:** Writing – review & editing; **Stefanie Reese:** Supervision, Funding acquisition; **Tim Brepols:** Writing – review & editing, Supervision, Funding acquisition.

Data availability

Data will be made available on request.

Declaration of competing interest

The authors declare that they have no known competing financial interests or personal relationships that could have appeared to influence the work reported in this paper.

Acknowledgements

Q. Zhang, T. Brepols, J. Kehls, and S. Reese acknowledge the financial support of subproject B05 within SFB/TRR 339 (project number: 453596084) by the German Research Foundation (DFG, Deutsche Forschungsgemeinschaft). J. Zhang acknowledges the financial support from the

China Scholarship Council (CSC). S. Ritzert, S. Reese, and T. Brepols acknowledge the financial support of the subproject A01 within SFB/TRR 280 (project number: 417002380) by the German Research Foundation (DFG, Deutsche Forschungsgemeinschaft).

Appendix A. Thermodynamic consistency and *two-surface* damage-plasticity

Here, consistent constitutive relations are derived using an extended form of the Clausius-Duhem inequality:

$$\mathbf{S} : \frac{1}{2}\dot{\boldsymbol{C}} + \underbrace{a_i\,\dot{\bar{D}} + \boldsymbol{b}_i \cdot \nabla\dot{\bar{D}}}_{\text{micromorphic extension}} - \dot{\psi} - \eta\,\dot{\theta} - \frac{1}{\theta}\,\boldsymbol{q}\cdot\nabla\theta \geq 0. \tag{A.1}$$

Inserting the time derivative of the Helmholtz free energy density function ψ (see Eq. (3)) into inequality (A.1), leads after some rearrangements to:

$$\begin{aligned}&\mathbf{S} : \frac{1}{2}\dot{\boldsymbol{C}} + \left(a_i - \frac{\partial\psi_{\bar{d}}}{\partial\bar{D}}\right)\dot{\bar{D}} + \left(\boldsymbol{b}_i - \frac{\partial\psi_{\bar{d}}}{\partial\nabla\bar{D}}\right)\cdot\nabla\dot{\bar{D}} - f_d(D)\left[\frac{\partial\psi_e}{\partial\boldsymbol{C}_e} : \dot{\boldsymbol{C}}_e + \frac{\partial\psi_p}{\partial\boldsymbol{C}_p} : \dot{\boldsymbol{C}}_p + \frac{\partial\psi_p}{\partial\xi_p}\,\dot{\xi}_p\right]\\ &-\left[\frac{\partial f_d(D)}{\partial D}\left(\psi_e + \psi_p\right) + \frac{\partial\psi_{\bar{d}}}{\partial D}\right]\dot{D} - \frac{\partial\psi_d}{\partial\xi_d}\,\dot{\xi}_d - \left(\frac{\partial\psi}{\partial\theta} + \eta\right)\dot{\theta} - \frac{1}{\theta}\,\boldsymbol{q}\cdot\nabla\theta \geqslant 0.\end{aligned} \tag{A.2}$$

By assuming a zero dissipation for the micromorphic (nonlocal) damage variable $\bar{D}$ and its gradient $\nabla\bar{D}$, the second Piola-Kirchhoff stress $\mathbf{S}$, the micromorphic forces (a_i, $\boldsymbol{b}_i$), the entropy η, and heat flux $\boldsymbol{q}$ are obtained:

$$\mathbf{S} = 2\,f_d(D)\,\frac{1}{\vartheta^2}\,\boldsymbol{F}_p^{-1}\,\frac{\partial\psi_e}{\partial\boldsymbol{C}_e}\,\boldsymbol{F}_p^{-\mathrm{T}},\quad a_i = \frac{\partial\psi_{\bar{d}}}{\partial\bar{D}},\quad \boldsymbol{b}_i = \frac{\partial\psi_{\bar{d}}}{\partial\nabla\bar{D}},\quad \eta = -\frac{\partial\psi}{\partial\theta},\quad \boldsymbol{q} = -\boldsymbol{K}_\theta\,\nabla\theta. \tag{A.3}$$

For brevity, the Mandel stress tensor $\boldsymbol{M}$ and the back stress tensor χ in the intermediate configuration are introduced as:

$$\boldsymbol{M} := 2\,f_d(D)\,\frac{\partial\psi_e}{\partial\boldsymbol{C}_e}\,\boldsymbol{C}_e,\quad \chi := 2\,f_d(D)\,\boldsymbol{F}_p^{\mathrm{T}}\,\frac{\partial\psi_p}{\partial\boldsymbol{C}_p}\,\boldsymbol{F}_p. \tag{A.4}$$

The conjugated driving forces to damage Y, isotropic hardening q_p, and damage hardening q_d are defined, respectively, as:

$$Y := -\left(\frac{\partial f_d(D)}{\partial D}\left(\psi_e + \psi_p\right) + \frac{\partial\psi_{\bar{d}}}{\partial D}\right),\quad q_p := f_d(D)\,\frac{\partial\psi_p}{\partial\xi_p},\quad q_d := \frac{\partial\psi_d}{\partial\xi_d}. \tag{A.5}$$

With Eqs. (A.3), (A.4), and (A.5), the remaining part of inequality (A.1) is reformulated as:

$$(\boldsymbol{M} - \chi) : \boldsymbol{D}_p - q_p\,\dot{\xi}_p - q_d\,\dot{\xi}_d + Y\,\dot{D} \geqslant 0, \tag{A.6}$$

where $\boldsymbol{D}_p = \frac{1}{2}\,\boldsymbol{F}_p^{-\mathrm{T}}\,\dot{\boldsymbol{C}}_p\,\boldsymbol{F}_p^{-1}$ represents the symmetric part of the plastic velocity gradient. The positive semi-definite conductivity tensor $\boldsymbol{K}_\theta$ in Eq. (A.3) is taken from Dittmann et al. (2020):

$$\boldsymbol{K}_\theta = \left(f_d(D)\,K_0 + \left(1 - f_d(D)\right)K_c\right)\boldsymbol{C}^{-1}. \tag{A.7}$$

K_0 and K_c denote the heat conduction parameters of the undamaged state ($f_d(D) = 1$) and fully broken state ($f_d(D) = 0$), respectively. Following Dittmann et al. (2020), as the temperature increases, the plastic material parameters are degraded by a thermal softening function $f_\theta(\theta)$ with a softening parameter ω:

$$f_\theta(\theta) = 1 - \omega\left(\theta - \theta_0\right). \tag{A.8}$$

Next, the plastic yield function Φ_p is employed using a von Mises-type criterion. Regarding damage, the damage loading function Φ_d is expressed as:

$$\Phi_p = \sqrt{\frac{3}{2}}\,\|\tilde{\boldsymbol{M}}' - \tilde{\chi}'\| - \left(\sigma_{y0} + \tilde{q}_p\right), \qquad \Phi_d = Y - \left(Y_0 + q_d\right). \tag{A.9}$$

Here, σ_{y0} denotes the initial yield stress. The operator $(\bullet)' = (\bullet) - \mathrm{tr}(\bullet)\,\boldsymbol{I}/3$ in Eq. (A.9) is the deviatoric part of a second-order tensor. $(\tilde{\bullet}) = (\bullet)/f_d(D)$ denotes an effective quantity. Y_0 represents the initial damage threshold.

- Plastic quantities

$$\boldsymbol{D}_p = \dot{\lambda}_p\,\frac{\partial \Phi_p}{\partial \boldsymbol{M}} = \dot{\lambda}_p\,\frac{1}{f_d(D)}\,\frac{\tilde{\boldsymbol{M}}' - \tilde{\chi}'}{\|\tilde{\boldsymbol{M}}' - \tilde{\chi}'\|}, \qquad \dot{\xi}_p = -\dot{\lambda}_p\,\frac{\partial \Phi_p}{\partial q_p} = \dot{\lambda}_p\,\frac{1}{f_d(D)} \tag{A.10}$$

The two variables $\dot{\lambda}_p$ and $\dot{\xi}_p$ denote the plastic multiplier and the accumulated plastic strain rate, respectively.

- Damage quantities

$$\dot{D} = \dot{\lambda}_d\,\frac{\partial \Phi_d}{\partial Y} = \dot{\lambda}_d, \qquad \dot{\xi}_d = -\dot{\lambda}_d\,\frac{\partial \Phi_d}{\partial q_d} = \dot{\lambda}_d \tag{A.11}$$

Here, $\dot{\lambda}_d$ represents the Lagrangian multiplier for the damage. According to Brepols et al. (2020), two sets of Karush-Kuhn-Tucker conditions are fulfilled as follows:

$$\begin{aligned} &\Phi_p \leq 0, \quad \dot{\lambda}_p \geq 0, \quad \dot{\lambda}_p\,\Phi_p = 0, \\ &\Phi_d \leq 0, \quad \dot{\lambda}_d \geq 0, \quad \dot{\lambda}_d\,\Phi_d = 0. \end{aligned} \tag{A.12}$$

Appendix B. Derivation of the internal energy

The Legendre transformation of the internal energy and its time derivative are defined as:

$$e_{\mathrm{int}} = \psi + \theta\,\eta, \quad \dot{e}_{\mathrm{int}} = \dot{\psi} + \dot{\theta}\,\eta + \theta\,\dot{\eta}. \tag{B.1}$$

By inserting the entropy $\eta = -\frac{\partial \psi}{\partial \theta}$ into Eq. (B.1), one obtains

$$e_{\mathrm{int}} = \psi + \theta\,\eta = \psi - \theta\,\frac{\partial \psi}{\partial \theta}. \tag{B.2}$$

After taking the partial derivative of Eq. (B.2) with respect to the temperature θ and integrating the obtained equation from the reference temperature θ_0 to the current temperature θ, the equation becomes

$$\frac{\partial e_{\mathrm{int}}}{\partial \theta} = \underbrace{-\theta\,\frac{\partial^2 \psi}{\partial \theta^2}}_{c} \quad \Rightarrow \quad e_{\mathrm{int}} = \int_{\theta_0}^{\theta} c\,d\theta + e_0, \tag{B.3}$$

where e_0 denotes the internal energy at temperature θ_0. Since the heat capacity c is assumed to be constant, the following result is obtained:

$$e_{\mathrm{int}} = c\,(\theta - \theta_0) + e_0, \quad \frac{d e_{\mathrm{int}}}{dt} = \frac{d}{dt}\left(c\,(\theta - \theta_0) + e_0\right) \quad \Rightarrow \quad \dot{e}_{\mathrm{int}} = c\,\dot{\theta}. \tag{B.4}$$

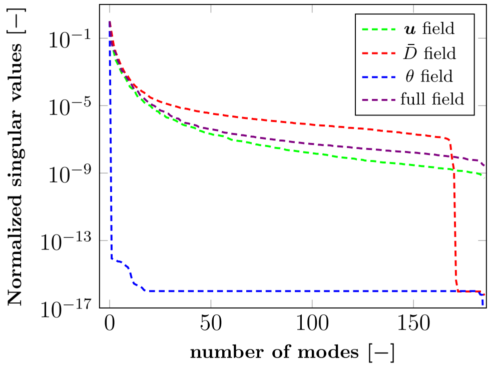

Fig. C.17. Distribution of normalized singular values of the asymmetrically notched specimen. The individual normalized singular values denote the displacement field $\boldsymbol{u}$, nonlocal damage field $\bar{D}$, and temperature field θ, see details in Zhang et al. (2025a).

Appendix C.

Here, a uniaxial tensile test conducted on an asymmetrically notched specimen is used to illustrate the slow decay of the singular values in the presence of damage simulations. As shown in Fig C.17, Fig. 4(a), and Fig. 9, the displacement and damage fields resulting from this test show complex localized features, leading to a slow decay in the distribution of singular values. These characteristics give rise to the Kolmogorov n-width approximation barrier when a linear projection-based model reduction approach is employed.

References

Ahmed, S.R., Ramm, G., Faltin, G., 1984. Some salient features of the time-averaged ground vehicle wake. SAE Trans., 473–503.
Ahrens, J., Geveci, B., Law, C., Hansen, C., Johnson, C., 2005. Paraview: an end-user tool for large-data visualization. Visualizat. Handbook 717, 717–731.
Ames, N.M., Srivastava, V., Chester, S.A., Anand, L., 2009. A thermo-mechanically coupled theory for large deformations of amorphous polymers. part II: applications. Int. J. Plast. 25 (8), 1495–1539.
An, S.S., Kim, T., James, D.L., 2008. Optimizing cubature for efficient integration of subspace deformations. ACM Trans. Graph. (TOG) 27 (5), 1–10.
Bachmayr, M., Cohen, A., 2017. Kolmogorov widths and low-rank approximations of parametric elliptic PDEs. Math. Comput. 86 (304), 701–724.
Barnett, J., Farhat, C., 2022. Quadratic approximation manifold for mitigating the Kolmogorov barrier in nonlinear projection-based model order reduction. J. Comput. Phys. 464, 111348.
Benner, P., Goyal, P., Heiland, J., Pontes Duff, I., 2023. A quadratic decoder approach to nonintrusive reduced-order modeling of nonlinear dynamical systems. PAMM 23 (1), e202200049.
Benner, P., Goyal, P., Kramer, B., Peherstorfer, B., Willcox, K., 2020. Operator inference for non-intrusive model reduction of systems with non-polynomial nonlinear terms. Comput. Methods Appl. Mech. Eng. 372, 113433.
Bhattacharjee, S., Matouš, K., 2016. A nonlinear manifold-based reduced order model for multiscale analysis of heterogeneous hyperelastic materials. J. Comput. Phys. 313, 635–653.
Brepols, T., Wulfinghoff, S., Reese, S., 2018. A micromorphic damage-plasticity model to counteract mesh dependence in finite element simulations involving material softening. Lect. Note. Appl. Comput. Mech. 86, 235–255.
Brepols, T., Wulfinghoff, S., Reese, S., 2020. A gradient-extended two-surface damage-plasticity model for large deformations. Int. J. Plast. 129, 102635.
Buffa, A., Maday, Y., Patera, A.T., Prud'Homme, C., Turinici, G., 2012. A priori convergence of the greedy algorithmfor the parametrized reduced basis method. ESAIM: Math. Modell. Numer. Anal. 46 (3), 595–603.
Bugas, D., Runnels, B., 2024. Grain boundary network plasticity: reduced-order modeling of deformation-driven shear-coupled microstructure evolution. J. Mech. Phys. Solids 184, 105541.
Chapman, T., Avery, P., Collins, P., Farhat, C., 2017. Accelerated mesh sampling for the hyper reduction of nonlinear computational models. Int. J. Numer. Methods Eng. 109 (12), 1623–1654.
Cohen, A., Farhat, C., Maday, Y., Somacal, A., 2023. Nonlinear compressive reduced basis approximation for PDE's. Comptes Rendus. Mécanique 351 (S1), 357–374.
Cordebois, J.P., Sidoroff, F., 1982. Damage induced elastic anisotropy. In: Mechanical Behavior of Anisotropic Solids/Comportment MÉchanique Des Solides Anisotropes. Springer, pp. 761–774.
Dittmann, M., Aldakheel, F., Schulte, J., Schmidt, F., Krüger, M., Wriggers, P., Hesch, C., 2020. Phase-field modeling of porous-ductile fracture in non-linear thermo-elasto-plastic solids. Comput. Methods Appl. Mech. Eng. 361, 112730.
Farhat, C., Avery, P., Chapman, T., Cortial, J., 2014. Dimensional reduction of nonlinear finite element dynamic models with finite rotations and energy-based mesh sampling and weighting for computational efficiency. Int. J. Numer. Methods Eng. 98 (9), 625–662.
Farhat, C., Chapman, T., Avery, P., 2015. Structure-preserving, stability, and accuracy properties of the energy-conserving sampling and weighting method for the hyper reduction of nonlinear finite element dynamic models. Int. J. Numer. Methods Eng. 102 (5), 1077–1110.
Fassin, M., Eggersmann, R., Wulfinghoff, S., Reese, S., 2019. Efficient algorithmic incorporation of tension compression asymmetry into an anisotropic damage model. Comput. Methods Appl. Mech. Eng. 354, 932–962.
Felder, S., Kopic-Osmanovic, N., Holthusen, H., Brepols, T., Reese, S., 2022. Thermo-mechanically coupled gradient-extended damage-plasticity modeling of metallic materials at finite strains. Int. J. Plast. 148, 103142.
Forest, S., 2009. Micromorphic approach for gradient elasticity, viscoplasticity, and damage. J. Eng. Mech. 135 (3), 117–131.
Gander, W., 1980. Algorithms for the QR decomposition. Res. Rep. 80 (02), 1251–1268.
Geelen, R., Balzano, L., Willcox, K., 2023a. Learning latent representations in high-dimensional state spaces using polynomial manifold constructions. In: 2023 62Nd IEEE Conference on Decision and Control (CDC). IEEE, pp. 4960–4965.
Geelen, R., Balzano, L., Wright, S., Willcox, K., 2024. Learning physics-based reduced-order models from data using nonlinear manifolds. Chaos: Interdiscip. J. Nonlinear Sci. 34 (3).
Geelen, R., Wright, S., Willcox, K., 2023b. Operator inference for non-intrusive model reduction with quadratic manifolds. Comput. Methods Appl. Mech. Eng. 403, 115717.
Ghavamian, F., Tiso, P., Simone, A., 2017. POD-DEIM Model order reduction for strain-softening viscoplasticity. Comput. Methods Appl. Mech. Eng. 317, 458–479.

Ghnatios, C., Cazacu, O., Revil-Baudard, B., Chinesta, F., 2024. A new methodology for anisotropic yield surface description using model order reduction techniques and invariant neural network. J. Mech. Phys. Solids 184, 105542.
Goodall, C.R., 1993. 13 Computation using the QR decomposition. In: Computational Statistics. Elsevier. Vol. 9 of *Handbook of Statistics*, pp. 467–508.
Gosea, I.V., Peterson, L., Goyal, P., Bremer, J., Sundmacher, K., Benner, P., 2023. Learning reduced-order quadratic-linear models in process engineering using operator inference. In: European Conference on Numerical Mathematics and Advanced Applications. Springer, pp. 365–376.
Goury, O., Duriez, C., 2018. Fast, generic, and reliable control and simulation of soft robots using model order reduction. IEEE Trans. Rob. 34 (6), 1565–1576.
Greif, C., Urban, K., 2019. Decay of the Kolmogorov n-width for wave problems. Appl. Math. Lett. 96, 216–222.
Grimberg, S., Farhat, C., Tezaur, R., Bou-Mosleh, C., 2021. Mesh sampling and weighting for the hyperreduction of nonlinear petrov-galerkin reduced-order models with local reduced-order bases. Int. J. Numer. Methods Eng. 122 (7), 1846–1874.
Grimberg, S., Farhat, C., Youkilis, N., 2020. On the stability of projection-based model order reduction for convection-dominated laminar and turbulent flows. J. Comput. Phys. 419, 109681.
Gruber, A., Tezaur, I., 2023. Canonical and noncanonical hamiltonian operator inference. Comput. Methods Appl. Mech. Eng. 416, 116334.
Grussler, C., Giselsson, P., 2018. Low-rank inducing norms with optimality interpretations. SIAM J. Optim. 28 (4), 3057–3078.
Halko, N., Martinsson, P.-G., Tropp, J.A., 2011. Finding structure with randomness: probabilistic algorithms for constructing approximate matrix decompositions. SIAM Rev. 53 (2), 217–288.
Hernandez, J.A., Caicedo, M.A., Ferrer, A., 2017. Dimensional hyper-reduction of nonlinear finite element models via empirical cubature. Comput. Methods Appl. Mech. Eng. 313, 687–722.
Hernández, J.A., Oliver, J., Huespe, A.E., Caicedo, M.A., Cante, J., 2014. High-performance model reduction techniques in computational multiscale homogenization. Comput. Methods Appl. Mech. Eng. 276, 149–189.
Jain, S., 2019. Some themes in nonlinear model reduction with applications to structural dynamics. Ph.D. thesis. ETH Zurich.
Jain, S., Tiso, P., 2019. Hyper-reduction over nonlinear manifolds for large nonlinear mechanical systems. J. Comput. Nonlinear Dyn. 14 (8), 081008.
Jain, S., Tiso, P., Rutzmoser, J.B., Rixen, D.J., 2017. A quadratic manifold for model order reduction of nonlinear structural dynamics. Comput. Struct. 188, 80–94.
Jiang, M., Zhang, Q., Zhang, S., Liu, M., Fu, Y., Zhang, Z., Ai, X., Mortazavi, B., Wang, L., Zhang, Q., et al., 2025. Microstructural transformation for robust and high-efficiency Zintl thermoelectrics. Nat. Commun. 16 (1), 7592.
Kaneko, S., Wei, H., He, Q., Chen, J.-S., Yoshimura, S., 2021. A hyper-reduction computational method for accelerated modeling of thermal cycling-induced plastic deformations. J. Mech. Phys. Solids 151, 104385.
Kastian, S., Kehls, J., Brepols, T., Reese, S., 2023. Discrete empirical interpolation method for nonlinear softening problems involving damage and plasticity. arXiv preprint arXiv:2311.17485
Kerfriden, P., Gosselet, P., Adhikari, S., Bordas, S. P.-A., 2011. Bridging proper orthogonal decomposition methods and augmented newton-krylov algorithms: an adaptive model order reduction for highly nonlinear mechanical problems. Comput. Methods Appl. Mech. Eng. 200 (5–8), 850–866.
Kerfriden, P., Goury, O., Rabczuk, T., Bordas, S. P.-A., 2013. A partitioned model order reduction approach to rationalise computational expenses in nonlinear fracture mechanics. Comput. Methods Appl. Mech. Eng. 256, 169–188.
Korelc, J., 2002. Multi-language and multi-environment generation of nonlinear finite element codes. Eng. Comput. 18, 312–327.
Korelc, J., Wriggers, P., 2016. Automation of Finite Element Methods. Springer.
Lange, N., Hütter, G., Kiefer, B., 2024. A monolithic hyper ROM FE^2 method with clustered training at finite deformations. Comput. Methods Appl. Mech. Eng. 418, 116522.
Lawson, C.L., Hanson, R.J., 1995. Solving least squares problems. SIAM.
Lee, J.A., Verleysen, M., 2007. Nonlinear dimensionality reduction. Springer Science & Business Media.
Liberty, E., Woolfe, F., Martinsson, P.-G., Rokhlin, V., Tygert, M., 2007. Randomized algorithms for the low-rank approximation of matrices. Proc. Natl. Acad. Sci. 104 (51), 20167–20172.
Lindsay, P., Fike, J., Tezaur, I., Carlberg, K., 2022. Preconditioned least-squares petrov-galerkin reduced order models. Int. J. Numer. Methods Eng. 123 (20), 4809–4843.
Lu, S.C.H., Pister, K.S., 1975. Decomposition of deformation and representation of the free energy function for isotropic thermoelastic solids. Int. J. Solids Struct. 11 (7–8), 927–934.
Mersel, L., Bouda, P., Germain, J., Réthoré, J., 2025. Dynamic damage modelling through phase-field approaches: assessment, critical analysis and comparison. Comptes Rendus. Mécanique 353 (G1), 687–724.
Michel, J.-C., Suquet, P., 2016. A model-reduction approach in micromechanics of materials preserving the variational structure of constitutive relations. J. Mech. Phys. Solids 90, 254–285.
Miehe, C., Hofacker, M., Welschinger, F., 2010. A phase field model for rate-independent crack propagation: robust algorithmic implementation based on operator splits. Comput. Methods Appl. Mech. Eng. 199 (45–48), 2765 - 2778.
Mishra, A., Carrara, P., Marfia, S., Sacco, E., De Lorenzis, L., 2024. Enhanced transformation field analysis for reduced-order modeling of problems with cohesive interfaces. Comput. Methods Appl. Mech. Eng. 421, 116755.
Narayan, S., Anand, L., 2021. Fracture of amorphous polymers: a gradient-damage theory. J. Mech. Phys. Solids 146, 104164.
Ohlberger, M., Rave, S., 2015. Reduced basis methods: Success, limitations and future challenges. arXiv preprint arXiv:1511.02021
Oliver, J., Caicedo, M., Huespe, A.E., Hernández, J.A., Roubin, E., 2017. Reduced order modeling strategies for computational multiscale fracture. Comput. Methods Appl. Mech. Eng. 313, 560–595.
Ostwald, R., Kuhl, E., Menzel, A., 2019. On the implementation of finite deformation gradient-enhanced damage models. Comput. Mech. 64 (3), 847–877.
de Parga, S.A., Bravo, J.R., Hernández, J.A., Zorrilla, R., Rossi, R., 2023. Hyper-reduction for petrov-galerkin reduced order models. Comput. Methods Appl. Mech. Eng. 416, 116298.
Parish, E.J., Rizzi, F., 2023. On the impact of dimensionally-consistent and physics-based inner products for POD-Galerkin and least-squares model reduction of compressible flows. J. Comput. Phys. 491, 112387.
Peherstorfer, B., 2020. Model reduction for transport-dominated problems via online adaptive bases and adaptive sampling. SIAM J. Sci. Comput. 42 (5), A2803–A2836.
Peherstorfer, B., 2022. Breaking the Kolmogorov barrier with nonlinear model reduction. Notic. Am. Math. Soc. 69 (5), 725–733.
Pinkus, A., 2012. N-widths in Approximation Theory. Vol. 7. Springer Science & Business Media.
Powell, M. J.D., 2004. Least frobenius norm updating of quadratic models that satisfy interpolation conditions. Math. Program. 100, 183–215.
Prume, E., Gierden, C., Ortiz, M., Reese, S., 2025. Direct data-driven algorithms for multiscale mechanics. Comput. Methods Appl. Mech. Eng. 433, 117525.
Qiao, H., Zhang, P., Wang, D., Zhang, B., 2012. An explicit nonlinear mapping for manifold learning. IEEE Trans. Cybern. 43 (1), 51–63.
Radermacher, A., Reese, S., 2013. A comparison of projection-based model reduction concepts in the context of nonlinear biomechanics. Arch. Appl. Mech. 83 (8), 1193–1213.
Radermacher, A., Reese, S., 2016. POD-Based model reduction with empirical interpolation applied to nonlinear elasticity. Int. J. Numer. Methods Eng. 107 (6), 477–495.
Reese, S., 2001. Thermomechanische Modellierung gummiartiger Polymerstrukturen. Institut für Baumechanik und Numerische Mechanik, Leibniz Universität Hannover.
Rocha, I.B., van der Meer, F.P., Mororó, L. A.T., Sluys, L.J., 2020. Accelerating crack growth simulations through adaptive model order reduction. Int. J. Numer. Methods Eng. 121 (10), 2147–2173.
Rokhlin, V., Szlam, A., Tygert, M., 2010. A randomized algorithm for principal component analysis. SIAM J. Matrix Anal. Appl. 31 (3), 1100–1124.
Ruan, H., Peng, X.-L., Yang, Y., Gross, D., Xu, B.-X., 2024. Phase-field ductile fracture simulations of thermal cracking in additive manufacturing. J. Mech. Phys. Solids 191, 105756.

Ruan, H., Rezaei, S., Yang, Y., Gross, D., Xu, B.-X., 2023. A thermo-mechanical phase-field fracture model: application to hot cracking simulations in additive manufacturing. J. Mech. Phys. Solids 172, 105169.
Rutzmoser, J., 2018. Model order reduction for nonlinear structural dynamics: simulation-free approaches. Ph.D. thesis. Technische Universität München.
Rutzmoser, J.B., Rixen, D.J., 2017. A lean and efficient snapshot generation technique for the hyper-reduction of nonlinear structural dynamics. Comput. Methods Appl. Mech. Eng. 325, 330–349.
Rutzmoser, J.B., Rixen, D.J., Tiso, P., Jain, S., 2017. Generalization of quadratic manifolds for reduced order modeling of nonlinear structural dynamics. Comput. Struct. 192, 196–209.
Ryckelynck, D., 2005. A priori hyperreduction method: an adaptive approach. J. Comput. Phys. 202 (1), 346–366.
Selvaraj, J., Hallett, S.R., 2024. Adaptive and variable model order reduction method for fracture modelling using explicit time integration. Comput. Methods Appl. Mech. Eng. 418, 116506.
Stojanovic, R., Djuric, S., Vujosevic, L., 1964. On finite thermal deformations. Archiwum Mechaniki Stosowanej 16, 103–108.
Taylor, R.L., 2014. FEAP - Finite Element Analysis Program.
Tezaur, R., As'ad, F., Farhat, C., 2022. Robust and globally efficient reduction of parametric, highly nonlinear computational models and real time online performance. Comput. Methods Appl. Mech. Eng. 399, 115392.
Trainotti, F., Marinko, J., Maierhofer, J., Rixen, D.J., 2024. ECSW Hyperreduction of hyper-viscoelastic components via co-simulation with abaqus. Finite Elem. Anal. Des. 241, 104222.
Unger, B., Gugercin, S., 2019. Kolmogorov n-widths for linear dynamical systems. Adv. Comput. Math. 45 (5), 2273–2286.
Volkwein, S., 2013. Proper orthogonal decomposition: theory and reduced-order modelling. Lect. Note. Univ. Konstanz 4 (4), 1–29.
Washabaugh, K., Amsallem, D., Zahr, M., Farhat, C., 2012. Nonlinear model reduction for CFD problems using local reduced-order bases. In: 42Nd AIAA Fluid Dynamics Conference and Exhibit, p. 2686.
Washabaugh, K.M., 2016. Faster fidelity for better design: A scalable model order reduction framework for steady aerodynamic design applications. Ph.D. thesis. Stanford University.
Wei, Z., Gerke, S., Brünig, M., 2023. Damage and fracture behavior under non-proportional biaxial reverse loading in ductile metals: experiments and material modeling. Int. J. Plast. 171, 103774.
Wei, Z., Gerke, S., Brünig, M., 2024. Numerical analysis of non-proportional biaxial reverse experiments with a two-surface anisotropic cyclic plasticity-damage approach. Comput. Methods Appl. Mech. Eng. 419, 116630.
Woolfe, F., Liberty, E., Rokhlin, V., Tygert, M., 2008. A fast randomized algorithm for the approximation of matrices. Appl. Comput. Harmon. Anal. 25 (3), 335–366.
Wu, J.-Y., 2017. A unified phase-field theory for the mechanics of damage and quasi-brittle failure. J. Mech. Phys. Solids 103, 72–99.
Wulfinghoff, S., 2025. Empirically corrected cluster cubature (E3C). Comput. Methods Appl. Mech. Eng. 437, 117779.
Zhang, Q., Mortazavi, B., Zhuang, X., Aldakheel, F., 2022. Exploring the mechanical properties of two-dimensional carbon-nitride polymer nanocomposites by molecular dynamics simulations. Compos. Struct. 281, 115004.
Zhang, Q., Ritzert, S., Zhang, J., Kehls, J., Reese, S., Brepols, T., 2025a. A multi-field decomposed model order reduction approach for thermo-mechanically coupled gradient-extended damage simulations. Comput. Methods Appl. Mech. Eng. 434, 117535.
Zhang, Q., Valizadeh, N., Liu, M., Zhuang, X., Mortazavi, B., 2025b. Hierarchical multiscale fracture modeling of carbon-nitride nanosheet reinforced composites by combining cohesive phase-field and molecular dynamics. Compos. Struct. 118942.
Zhang, Q., Zhang,J., Reese, S., Brepols, T., 2024. A nonlinear manifold model order reduction approach for thermo-mechanically coupled plasticity. PAMM, e202400070.